https://doi.org/10.1016/j.cemconcomp.2022.104896

Tensile Over-Saturated Cracking of Ultra-High-Strength Engineered Cementitious Composites (UHS-ECC) with Artificial Geopolymer Aggregates

Ling-Yu Xu [1]*; Bo-Tao Huang* [2] *(*); Jian-Cong Lao* [3]*; Jie Yao* [4]*;*
Victor C. Li [5]*; Jian-Guo Dai* [6] *(*)*

Highlights

- UHS-ECC with artificial geopolymer aggregates (GPA) were developed with both ultra-high strength (over 150 MPa) and ultra-high ductility (over 8%).
- Over-saturated cracking was observed in UHS-ECC with GPA size smaller than 0.60 mm.
- UHS-ECC with over-saturated cracking exhibited a double-stage crack evolution.
- The mechanism of the over-saturated cracking of the GPA-based UHS-ECC is revealed.
- UHS-ECC with GPA size of 0.30–0.60 mm exhibited the highest strain-hardening potential.

---

[1] Ph.D., Department of Civil and Environmental Engineering, The Hong Kong Polytechnic University, Hong Kong, China. E-mail: ling-yu.xu@connect.polyu.hk

[2] ZJU100 Young Professor, Institute of Advanced Engineering Structures, Zhejiang University, Hangzhou, China; Research Fellow, Department of Civil and Environmental Engineering, The Hong Kong Polytechnic University, Hong Kong, China. E-mail: botaohuang@zju.edu.cn (**Corresponding Author*)

[3] Research Associate, Department of Civil and Environmental Engineering, The Hong Kong Polytechnic University, Hong Kong, China. E-mail: Attic.lao@connect.polyu.hk

[4] Engineer, China State Construction Hailong Technology Company Ltd., Shenzhen, China, Email: jyaoad@connect.ust.hk

[5] Professor, Department of Civil and Environmental Engineering, University of Michigan, Ann Arbor, USA. E-mail: vcli@umich.edu

[6] Professor, Department of Civil and Environmental Engineering, The Hong Kong Polytechnic University, Hong Kong, China. E-mail: cejgdai@polyu.edu.hk (**Corresponding Author*)

Abstract

Ultra-High-Strength Engineered Cementitious Composites (UHS-ECC) incorporating artificial geopolymer aggregates (GPA) were developed and over-saturated cracking (i.e., average tensile crack spacing smaller than the theoretical limit) was observed in this novel material. The developed UHS-ECC exhibited an ultra-high compressive strength (over 150 MPa) and an ultra-high tensile ductility (over 8%) simultaneously. The influences of GPA size on the matrix properties, tensile performance, micromechanics, and cracking behavior of UHS-ECC were systematically investigated. Over-saturated cracking and double-stage crack evolution (i.e., a bilinear relation between average crack width and tensile strain) were observed in UHS-ECC with GPA size smaller than 0.60 mm, while saturated cracking and single-stage crack evolution (i.e., a linear relation between average crack width and tensile strain) were observed in the other groups. Finally, the mechanism of over-saturated cracking and double-stage crack evolution was illustrated. The findings of this study extend the fundamental knowledge of ECC technology, which is meaningful for designing and developing UHS-ECC materials towards ultra-high tensile ductility.

Keywords

Engineered Cementitious Composites (ECC); Strain-hardening Cementitious Composites (SHCC); Ultra-High-Performance Concrete (UHPC); Geopolymer; Alkali--activated material; Artificial aggregate; Multiple cracking

Graphical Abstract

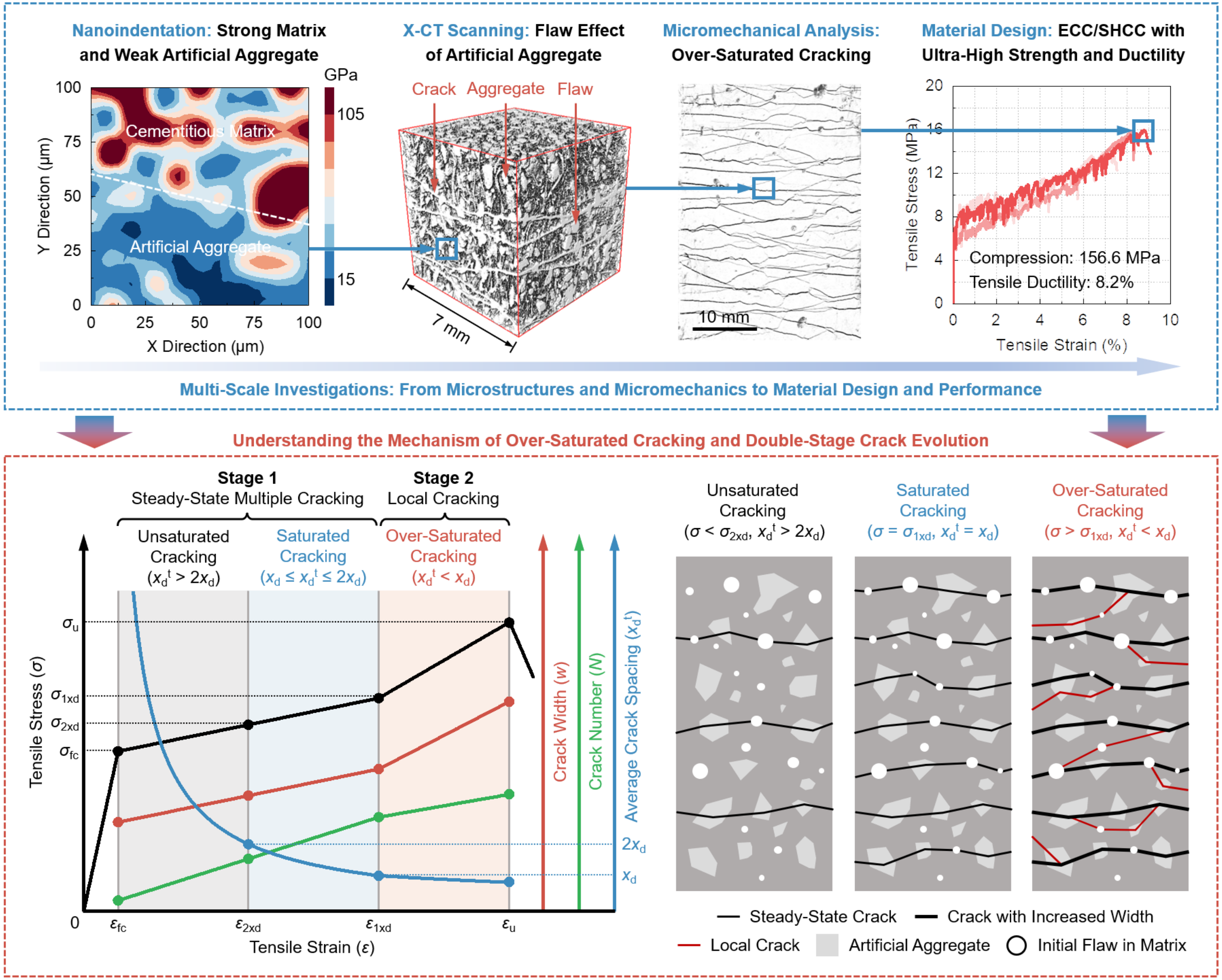

1 Introduction

Engineered/Strain-Hardening Cementitious Composites (ECC/SHCC) are advanced fiber-reinforced cement-based materials with high/ultra-high tensile ductility (typically 2–10%) and saturated multiple cracking behavior [1, 2, 3, 4, 5], which can be regarded as a special category of fiber-reinforced concrete [6, 7, 8, 9]. ECC materials normally show a compressive strength ranging from 20 MPa to 80 MPa (similar to ordinary concrete) [10, 11, 12, 13] and have been successfully applied in building, transportation, and hydraulic infrastructures [1, 14, 15]. In the recent decade, two new categories of ECC with superior mechanical performance have been designed and developed [i.e., high-strength ECC (HS-ECC, 80–150 MPa in compression) and ultra-high-strength ECC (UHS-ECC, 150–210 MPa in compression)] [16, 17, 18, 19]. Owing to the excellent mechanical performance and dense microstructures, HS/UHS-ECC have great potential in developing more resilient and durable infrastructure under complex loading and environmental conditions. It is worth mentioning that some existing ultra-high-performance concrete (UHPC) [21, 22, 23, 24, 25] also showed tensile strain-hardening behavior in spite of the relatively low strain capacity (e.g., below 1%) [26, 27, 28]. Actually, UHS-ECC could also be regarded as a special category of strain-hardening UHPC with a significantly higher tensile ductility (e.g., > 3%).

In the matrix design of HS/UHS-ECC, ultra-fine silica sand (typically smaller than 300 μm) is widely used to meet the micromechanical guidelines of strain-hardening cementitious composites [1, 29, 30]. It should be pointed out that ultra-fine silica sand is much more expensive than the river sand used in ordinary concrete [31], and the production of silica sand consumes natural silica rocks. To reduce the material cost, both coarse river sand and sea sand have been used to fully replace silica sand in HS-ECC production [32, 33, 34, 35]. It was found that the increase of the sea-sand size resulted in the decreased compressive and tensile strengths, while the tensile strain capacity of HS-ECC was little influenced [35].

Artificial geopolymer aggregates (GPA) are emerging as a sustainable alternative to replace natural aggregates in cementitious materials [36, 37, 38]. Similar to the traditional geopolymer materials [39, 40, 41, 42], GPA are commonly made from industrial/urban wastes/by-products. Thus, they have gradually become popular in recent years owing to their one-stone-for-two-birds potential to simultaneously relieve environmental burdens of waste accumulation and natural aggregate over-exploitation [43, 44]. The existing GPA technologies could be classified into three categories: sintered aggregates [45, 46], traditional cold-bonded aggregates (usually known as cement-bonded aggregates) [47, 48, 49], and GPA [50, 51]. Different from natural aggregates with high rigidity, GPA commonly show a lower stiffness and fracture energy. Therefore, they could be considered as "flaws" in the high-strength cementitious matrix. It should be pointed out that according to the micromechanical design guideline of ECC, the addition of suitable artificial flaws can tailor the multiple cracking behavior of ECC [1, 52, 53, 54]. Very recently, the authors successfully utilized GPA as artificial flaws to develop HS-ECC with ultra-high tensile ductility (compressive strength > 120 MPa; tensile ductility > 8%) [55, 56]. In this preliminary work, the GPA were found to react with cementitious matrix (blended cement and silica fume) when GPA with the maximum particle size of 4.75 mm were used for HS-ECC production [55, 56, 57, 58].

It is well known that the mechanical properties of ECC materials are influenced by the aggregate size. The natural aggregates with larger size increase the matrix fracture toughness and non-uniformity of fiber distribution in ECC [1, 4, 35], leading to inferior tensile performance. However, these findings were obtained based on highly rigid natural aggregates, but GPA are much weaker, which may have different effects on ECC's performance. In addition, natural aggregates are usually inert in the cement matrix, while it is possible for finer GPA (with larger specific surface area) to behave like a pozzolanic reactant to accelerate the matrix hydration. More importantly, the flaw distribution of matrix is highly related to the size of GPA, which influences the multiple cracking behavior of ECC (e.g., crack width, spacing, and branching). In summary, the GPA size is an important factor influencing the properties of GPA-based ECC, including hydration process, micromechanics, tensile performance, and cracking behavior. Thus, an in-depth understanding of how the GPA size influences ECC properties is critical for the material design and optimization. Particularly, the fundamental knowledge on optimizing the interaction between GPA and ECC is very useful for improving the tensile strain capacity of HS/UHS-ECC.

In this study, GPA with different particle sizes (i.e., < 0.30 mm, 0.30–0.60 mm, 0.60–1.18

mm, and 1.18–2.36 mm) were used as fine aggregates to develop UHS-ECC with ultra-high tensile ductility. A comprehensive multi-scale investigation was conducted to understand the effects of GPA size on the properties of UHS-ECC. The mechanical properties of the GPA-based UHS-ECC were investigated, and a control mix with fine silica sand was used as the comparison. Then, the hydration and microstructures of the UHS-ECC matrix were analyzed based on the calorimetry test, nanoindentation, and X-ray computed tomography (XCT)., and micromechanical tools were utilized to understand the tensile strain-hardening behavior. Emphasis was placed on the multiple cracking process of the GPA-based UHS-ECC showing over-saturated cracking (i.e., the average tensile crack spacing is smaller than the theoretical limit) and double-stage crack evolution. The micromechanical mechanism of over-saturated cracking was analyzed. Finally, the desirable particle size of GPA to enhance the tensile performance of UHS-ECC was suggested. The findings extend the fundamental knowledge of ECC technology and provide a new avenue to designing and developing ECC with both ultra-high strength and ultra-high ductility.

2 Experimental programs

2.1 Raw materials

Coal fly ash (FA), Type I 52.5 N Portland cement, ground granulated blast-furnace slag (GGBS), and silica fume (SF) were used as the raw materials for GPA and UHS-ECC production. The chemical components and loss on ignition (LOI) values of these materials obtained from X-ray fluorescence (XRF) tests are presented in **Table 1**. From the obtained Al_2O_3, SiO_2, CaO, and Fe_2O_3 contents, the FA can be classified as Class F according to ASTM C618-19 [59]. GGBS had high SiO_2 and CaO contents, while SF is almost silicious. It should be noted here that the negative LOI of GGBS is caused by the oxidation of sulfur-rich species [60]. Quartz powder (QP) with SiO_2 content of 98.6% was used in UHS-ECC matrix [61, 62]. The detailed particle size distributions of raw materials are shown in **Fig. 1**.

Table 1 Chemical components and LOI values of raw materials obtained from XRF (%).

Chemical Composition	FA	GGBS	Cement	SF
Aluminum Oxide, Al_2O_3	25.80	14.60	6.07	0.15
Silicon Oxide, SiO_2	52.40	33.90	19.60	96.90

Calcium Oxide, CaO	6.42	40.50	64.80	0.53
Ferric Oxide, Fe_2O_3	8.40	0.30	3.01	0.06
Magnesium Oxide, MgO	2.27	7.03	0.87	1.10
Sulfur Trioxide, SO_3	0.86	2.23	4.24	0.12
Titanium Dioxide, TiO_2	1.31	0.51	0.26	/
Phosphorus Oxide, P_2O_5	0.66	0.13	0.13	0.33
Potassium Oxide, K_2O	1.47	0.46	0.68	0.78
Others	0.41	0.34	0.34	0.03
LOI (950 °C)	3.48	-0.14	3.83	1.78

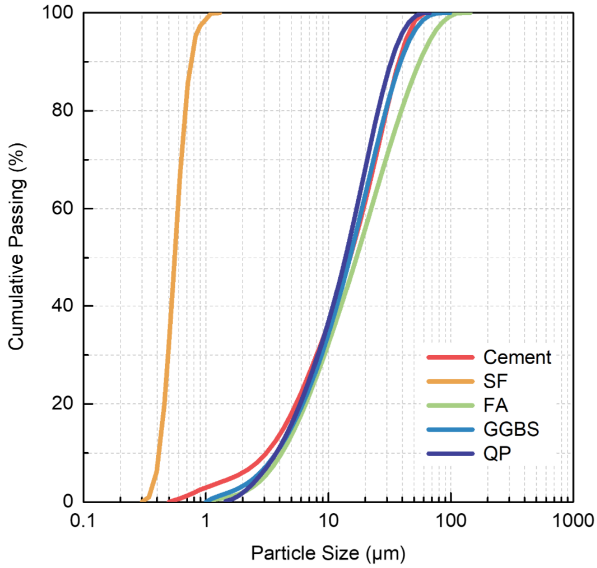

Fig. 1 Particle size distributions of raw materials for the production of GPA and UHS-ECC.

Anhydrous sodium metasilicate (Na_2SiO_3-Anhydrous) particles (in industrial grade) with the chemical components of 50.75% Na_2O, 46.52% SiO_2, and 2.73% impurities were used as the solid alkaline activator for GPA production. The solid activator had the particle size of 0.25–1.00 mm and the loose bulk density of 1.31 g/cm^3 (provided by the supplier).

Fine silica sand (FSS) with particle size smaller than 0.3 mm was used in the FSS-based UHS-ECC. According to GB/T 14684-2011 [63], the water absorption and specific gravity of FSS were tested as 0.8% and 2.67, respectively.

Ultra-high-molecular-weight polyethylene (PE) fibers were used as the fiber reinforcement [64, 65]. The strength, modulus, density, diameter, and length of the PE fibers were 3000 MPa, 100 GPa, and 0.97 g/cm^3, 24 μm, and 18 mm, respectively.

Polycarboxylate ether type super-plasticizer (SP) provided by BASF Hong Kong was adopted to reduce the water demand for UHS-ECC in this study.

2.2 Artificial geopolymer aggregates (GPA)

As the first step of GPA production, one-part mixing (i.e., just add water) method was adopted to prepare geopolymer pastes [44]. The mix proportion of GPA is presented in **Table 2**. During the mixing procedure, the solid materials (FA, GGBS, and Na_2SiO_3-Anhydrous) were firstly put together into a mixer and dry-mixed for 5 min before the water was added. Then, the slurry was continuously stirred for another 4 min, and the obtained uniform geopolymer paste was poured into 100 mm × 100 mm × 100 mm cubic molds, vibrated for 30 s, and then covered with plastic sheets to prevent water evaporation. After the initial curing of 24 h, the specimens were demolded and crushed into fragments smaller than 4.75 mm using a crushing machine. Afterwards, the GPA with different particle sizes (< 0.30 mm, 0.30–0.60 mm, 0.60–1.18 mm, and 1.18–2.36 mm) were sieved, collected and stored in different sealed plastic bags for six months. The photographs of GPA with different particle sizes are shown in **Fig. 2**. It is noted that as a newly-developed material, an in-depth understanding of the role of GPA size in ductility enhancement mechanism is critical for the design and optimization of GPA-ECC. Thus, this study selected the four specific size intervals of GPA (i.e., < 0.30 mm, 0.30–0.60 mm, 0.60–1.18 mm, and 1.18–2.36 mm) to understand which size range could contribute most to the tensile performance. Following the same testing procedures in Ref. [56], the specific gravity, water absorption and water content of the produced GPA were 2.05, 19.2%, and 24.6%, respectively. In addition, the 28-day strength of GPA was 52.4 MPa through testing the 20 mm × 20 mm × 20 mm geopolymer cubes with the same mix proportion and curing condition.

Table 2 Mix proportion of GPA (kg/m^3).

Raw Materials	Mix Proportion
FA	1019.3
GGBS	254.8
Na_2SiO_3-Anhydrous	152.9
Water	446.0

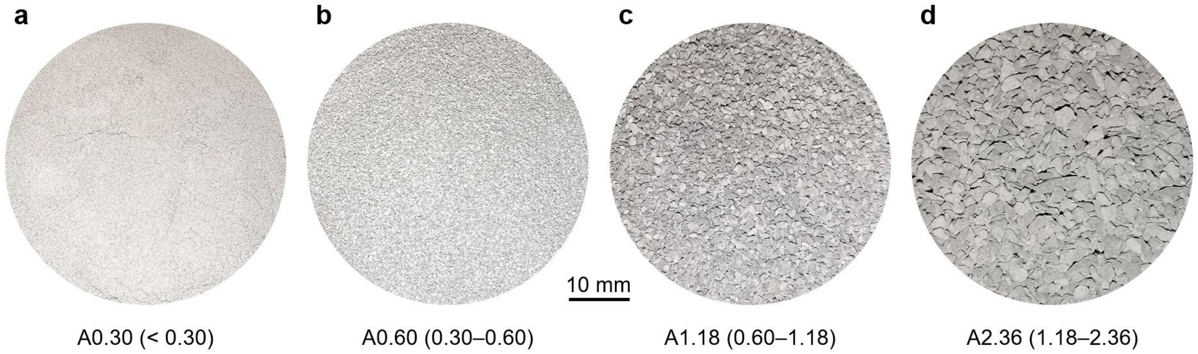

Fig. 2 Photographs of artificial aggregates with different particle sizes: (a) < 0.30 mm (A0.30), (b) 0.30–0.60 mm (A0.60), (c) 0.60–1.18 mm (A1.18), and (d) 1.18–2.36 mm (A2.36).

2.3 UHS-ECC

Four mix proportions of UHS-ECC with different GPA sizes (i.e., < 0.30 mm for A0.30, 0.30–0.60 mm for A0.60, 0.60–1.18 mm for A1.18, and 1.18–2.36 mm for A2.36) and one mix proportion of UHS-ECC with FSS (Mix ID: F0.30) were prepared in this study (**Table 3**). The weight ratios of GPA were kept the same for all the GPA-based UHS-ECC. For the FSS-based UHS-ECC, the volume ratio of FSS were kept the same with that of GPA in GPA-based UHS-ECC (calculated by the specific gravity of dry aggregates).

Table 3 Mix proportion of UHS-ECC (kg/m^3).

UHS-ECC	Mix IDs	Binder Materials			QP	Aggregates SSD (Dry)		Water	SP (In solid)	PE Fibers
		Cement	SF	GGBS		FSS	GPA			
GPA-based UHS-ECC	A0.30 A0.60 A1.18 A2.36	1069.0	267.2	133.6	133.6	/	320.7 (257.4)	232.9	25.0	19.4 (2% Vol.)
FSS-based UHS-ECC	F0.30	1136.6	284.1	142.1	142.1	358.8 (356.0)	/	247.6	26.6	19.4 (2% Vol.)

For each mix proportion, the following steps were taken during the ECC preparation procedure. Firstly, GPA (FSS) were pre-wetted to saturated surface dry (SSD) condition based on the tested initial water content and water absorption ratio. Then, the binder materials and SSD GPA (FSS) were dry-mixed for 5 min. Next, water and SP were added into the mixture, followed by continuous stirring for another 10 min. After a uniform fresh paste was formed, PE fibers were slowly added into the mixture with continued stirring for 5 min. Finally, the fresh ECC were cast into cubic and dumbbell molds, and sealed with plastic sheets to prevent water evaporation. Demolding was conducted after 48 h, and the demolded specimens were heat-cured in 90 °C water for 7 d to accelerate the hydration of the cementitious paste [19]. After heat curing, the UHS-ECC specimens were dried at the room temperature of 23 °C for 48 h for further tests. It is noted that the mini-slump spread diameter of the fresh UHS-ECC was measured according to ASTM C1437 [66], and the spread diameters of F0.30, A2.36, A1.18, A0.60, and A0.30 were 131, 132, 129, 125, and 121 mm, respectively. It can be seen that the workability of the GPA-based UHS-ECC decreased with decreasing GPA size. The air contents of the fresh mixtures of F0.30, A2.36, A1.18, A0.60, and A0.30 were 4.0%, 4.2%, 4.3%, 4.6% and 4.9%, respectively, according to GB/T 50080-2016 [67]. For the GPA-based UHS-ECC, the air content increased with the decrease of GPA size. Also, the measured densities of the freshly-mixed UHS-ECC for F0.30, A2.36, A1.18, A0.60, and A0.30 were 2268, 2143, 2148, 2145, and 2153 kg/m^3, respectively.

2.4 Testing methods

<u>*Compression and direct tension.*</u> For each mix proportion, three 50 mm × 50 mm × 50 mm UHS-ECC cubes were tested under compression. The loading rate was 1.0 MPa/s. Three dumbbell specimens were tested under direct tension with the loading rate of 0.5 mm/min for each mix proportion (see **Fig. 3a**) [68, 69]. Two linear variable differential transformers (LVDTs) were utilized to measure the deformation of UHS-ECC with a gauge length of 80 mm. Furthermore, in order to capture the multiple cracking process during the test, a digital camera was utilized to capture the photographs of the specimen surface at an interval of three seconds. The compressive and direct tensile tests were conducted for all the UHS-ECC mixes in **Table 3** (i.e., both FSS- and GPA-based UHS-ECC), and the following tests were conducted for GPA-based UHS-ECC.

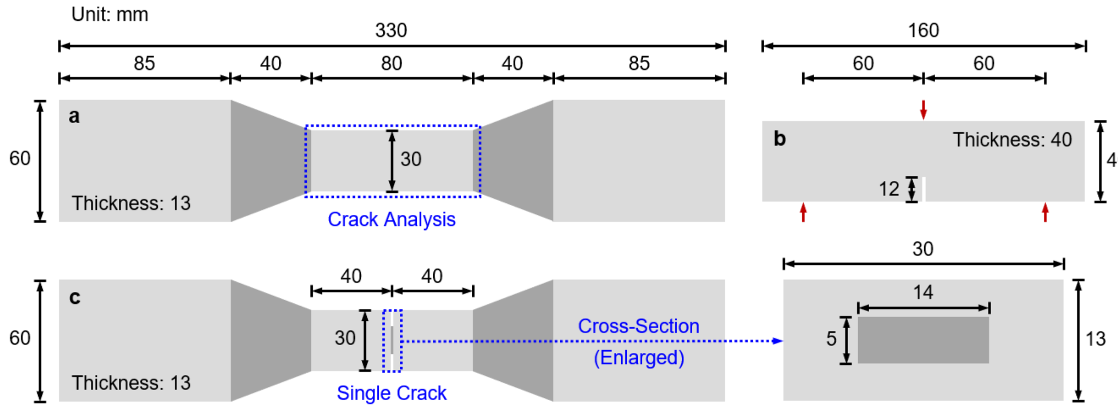

Fig. 3 Dimensions of specimens for (a) direct tensile test, (b) fracture toughness test, and (c) single-crack tensile test.

Hydration heat. Isothermal calorimetry tests were carried out to evaluate the influence of the GPA size on the hydration process of the ECC matrix (excluding fibers). The fresh samples were prepared with the same mixing process as presented in *Section 2.3*, and then they were weighed and placed in an isothermal calorimetry machine (Calmetrix I-Cal 4000) for 48 h. The measured hydration heat was normalized by the matrix weight for the analysis.

Nanoindentation. For the nanoindentation test (Hysitron TI Premier, Bruker), one 40 mm × 40 mm × 40 mm cubic ECC sample (A0.60) was prepared and cured under the same regime as described in *Section 2.3*. After that, a small piece was cut from the cube and fixed in the hardened epoxy resin. The sample was first polished using SiC abrasive grinding papers (180, 240, 600, 800, and 1200 grit) for a total procedure of 3 h. Then, a delicate polishing process was conducted for another 30 min using finer grinding papers (3, 1, and 0.25 μm) sprayed with oil-based diamond suspensions. For the nanoindentation test, 121 indents were conducted (11 × 11 grid with a 10 μm spacing). For each indent, the load was increased to 2 μN in 5 s, held for 2 s, and then reduced to zero in 5 s. The Poisson's ratios of both cementitious paste and GPA were assumed as 0.2. The elastic modulus and the hardness were calculated based on the Oliver and Pharr method [70, 71].

X-ray CT scanning. After the direct tensile tests, small pieces cut from the middle part of the dumbbell specimens were scanned by a micro-focus X-ray CT system (YXLON FF35 CT) with a voxel size of 10.3 μm.

<u>*Matrix elastic modulus.*</u> Three replicate cylindrical specimens of the UHS-ECC matrix (excluding fibers) with a diameter of 50 mm and a height of 100 mm were prepared for each mix proportion with the same mixing and curing procedure as described in *Section 2.3*. The testing procedure of the elastic modulus followed ASTM C469/C469M-14 [72]. Two strain gauges with a gauge length of 50 mm were utilized to measure the axial deformation of the specimens under compression. The loading rate was set as 1.0 mm/min.

<u>*Matrix fracture toughness.*</u> Three 40 mm × 40 mm × 160 mm notched specimens of the UHS-ECC matrix (excluding fibers) were prepared (12-mm notch at the mid-span of the specimen). The dimension of the tested specimens can be seen in **Fig. 3b**. The three point-bending test was conducted with a loading rate of 0.2 mm/min.

<u>*Single-crack behavior.*</u> Two additional dumbbell UHS-ECC specimens were prepared following the procedure in *Section 2.3*. A circumferential notch was carefully prefabricated, and the dimension of the specimen is presented in **Fig. 3c**. During the test, the notch opening was monitored. The loading rate of the single-crack tensile test was the same as that adopted in the direct tensile test (i.e., 0.5 mm/min).

3 Mechanical performance of UHS-ECC

3.1 Compressive strength

The compressive strengths of UHS-ECC with different GPA sizes are summarized in **Fig. 4a**. It can be seen that the compressive strength of FSS-based UHS-ECC was larger than that of the GPA-based UHS-ECC, owing to the lower mechanical strength of GPA. Among all the GPA-based UHS-ECC mixes, A0.30 showed the highest compressive strength of 165.6 MPa due to a more complete hydration reaction occurred in this mix, and this argument will be supported by the results of the isothermal calorimetry test in *Section 4.1*. The compressive strength of UHS-ECC gradually decreased with the increasing GPA size. This phenomenon was also related to the fact that the larger GPA would lead to a more pronounced stress localization in the ultra-high-strength matrix. Although the GPA used were much weaker than the cementitious matrix, all the GPA-based UHS-ECC showed an ultra-high compressive strength ranging from 147.4 MPa to 165.6 MPa. The tensile performance of the UHS-ECC presented in

Fig. 4b–d will be discussed in the next section.

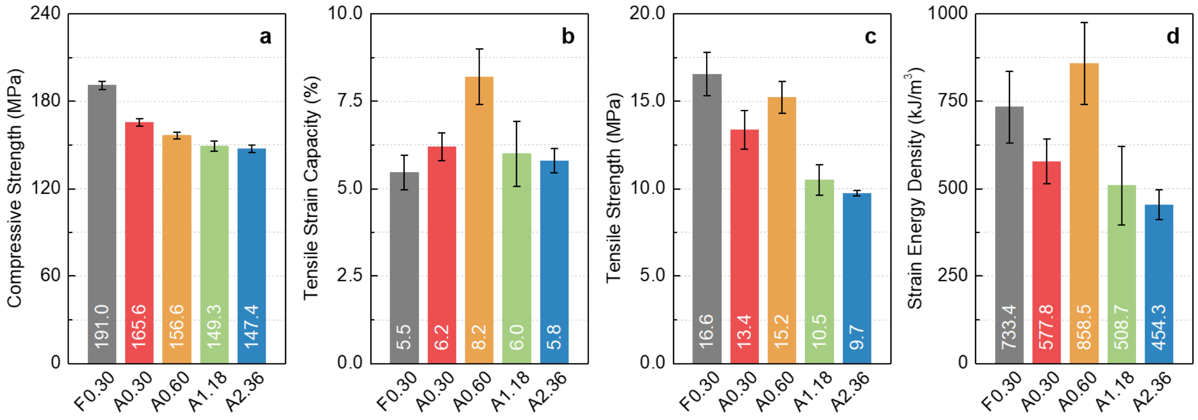

Fig. 4 Summary of the mechanical properties of UHS-ECC: (a) Compressive strength, (b) tensile strain capacity, (c) tensile strength, and (d) tensile strain energy density.

3.2 Tensile strain-hardening behavior

Fig. 5 shows the tensile stress-strain curves of UHS-ECC with different GPA sizes, and the tensile properties are summarized in **Fig. 4b–d**. It can be found that FSS-based UHS-ECC showed the highest tensile strength (i.e., 16.6 MPa) but the lowest tensile strain capacity (i.e., 5.5%). In addition, the tensile strain energy density of the FSS-based UHS-ECC was 733.4 kJ/m^3. Among the developed GPA-based UHS-ECC, A0.60 showed higher tensile strain capacity (i.e., 8.2% in **Fig. 4b**), tensile strength (i.e., 15.2 MPa in **Fig. 4c**), and strain energy density (i.e., 858.5 kJ/m^3 in **Fig. 4d**), indicating that the GPA size of 0.30–0.60 mm was the most suitable for achieving ultra-high tensile ductility in UHS-ECC.

The GPA larger than 0.60 mm (i.e., A1.18 and A2.36) may not distribute as uniformly as those in A0.60, because the number of GPA decreased significantly with the increasing GPA size. This argument will also be supported by the XCT results in *Section 5.1*. The use of larger size GPA would disturb the uniform distribution of fibers [35] and thus reduce the tensile strength of UHS-ECC (see **Fig. 4c**). The non-uniform distribution of GPA also resulted in a larger variation of matrix fracture toughness. Some of GPA smaller than 0.30 mm could be considered as powders (binder material), while the others were aggregates. As a result, part of the GPA did not work as "additional flaws" in the UHS-ECC matrix due to their small particle size, leading to a lower tensile strain capacity of A0.30 than that of A0.60.

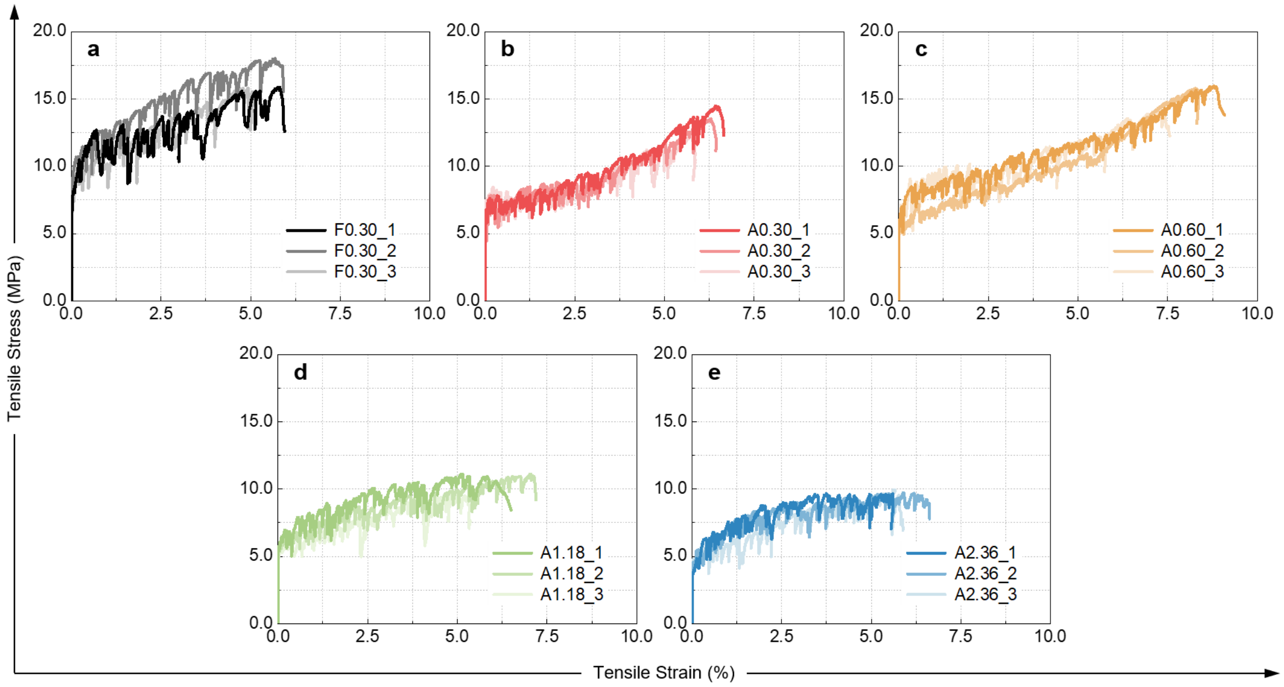

Fig. 5 Tensile stress–strain relations of UHS-ECC: (a) F0.30, (b) A0.30, (c) A0.60, (d) A1.18, and (e) A2.36.

All the UHS-ECC mixes exhibited distinguished strain-hardening behaviors, which is similar to normal-strength ECC materials [73, 74]. However, for the GPA-based UHS-ECC, significant differences were observed between the tensile stress-strain curves of the mixes with smaller GPA (i.e., A0.30 and A0.60) and the mixes with larger GPA (i.e., A1.18 and A2.36). For the strain-hardening parts of A0.30 and A0.60, two segments existed and the slope of the second part was larger than that of the first part, while for A1.18 and A2.36, the trend was opposite. This interesting phenomenon is in fact related to the over-saturated cracking mechanism, which will be analyzed in the following sections using micromechanical tools.

3.3 Crack pattern

Fig. 6 shows the typical crack patterns of UHS-ECC. Compared with the FSS-based UHS-ECC (i.e., F0.30 in **Fig. 6a**), the GPA-based UHS-ECC showed a significantly smaller crack spacing, indicating the contribution of GPA in the multiple cracking process. It can also be seen that UHS-ECC with the larger GPA sizes showed a more non-uniform cracking behavior. Although larger GPA could function as additional flaws more effectively, the corresponding number of GPA is reduced with increasing size. Compared with A0.30 and A0.60, the nonuniformly-distributed GPA in A1.18 and A2.36 led to more localized crack distributions (**Fig. 6d**–**e**). On the other hand, although GPA smaller than 0.30 mm (A0.30) distributed more evenly in the UHS-ECC matrix, some GPA would only work as binder materials instead of artificial flaws, and could not induce cracks effectively. Therefore, the most saturated cracking condition was observed in A0.60 (**Fig. 6c**), which was also in accordance with the highest tensile strain capacity (i.e., 8.2%) of this mix in **Fig. 4b**.

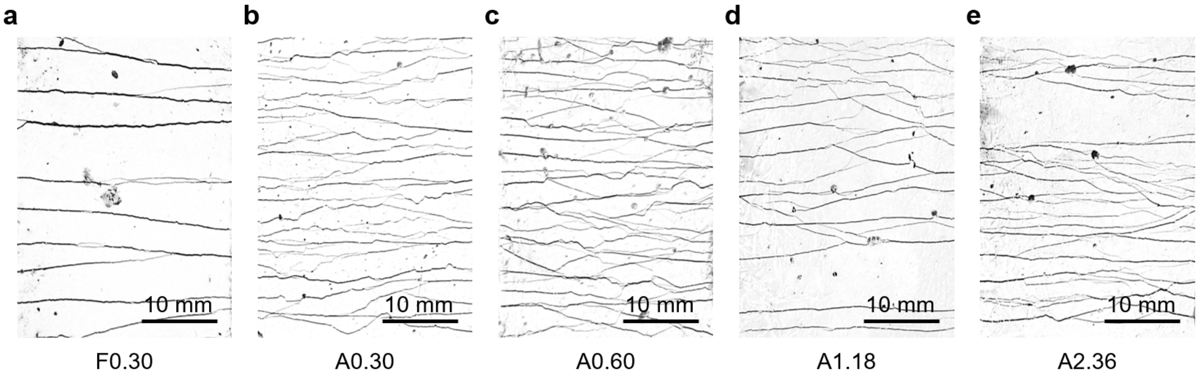

Fig. 6 Crack patterns of UHS-ECC at the ultimate tensile strain: (a) F0.30, (b) A0.30, (c) A0.60, (d) A1.18, and (e) A2.36.

4 Matrix characteristics of UHS-ECC with Artificial Aggregates

4.1 Hydration heat

The heat release rate and cumulative heat of UHS-ECC matrices with different GPA sizes during the first 48 h hydration process are presented in **Fig. 7**. Since GPA reacted with the cementitious paste [56], the UHS-ECC matrix using finer GPA could generate higher cumulative heat due to the larger specific surface area of finer GPA. For GPA size above 1.18 mm, little difference was observed in the heat release curves of UHS-ECC matrices (i.e., A1.18 and A2.36 in **Fig. 7**). It indicated that the GPA with small specific surface areas showed limited reactivity and functioned more likely as fillers in the cementitious matrix. On the other hand, when the upper limit of the GPA size was reduced to 0.60 mm, the peak of the heat release rate moved towards the upper left of **Fig. 7**. It is inferred that the unreacted raw materials (FA and GGBS) existing in GPA could also consume the $Ca(OH)_2$ generated during the cement hydration, which accelerated the hydration procedure and released more reaction heat. In addition, the Na_2SiO_3-Anhydrous particles possibly remained undissolved during the one-part mixing of GPA might also react with FA and GGBS again in the fresh cementitious paste and promote the heat generation [56].

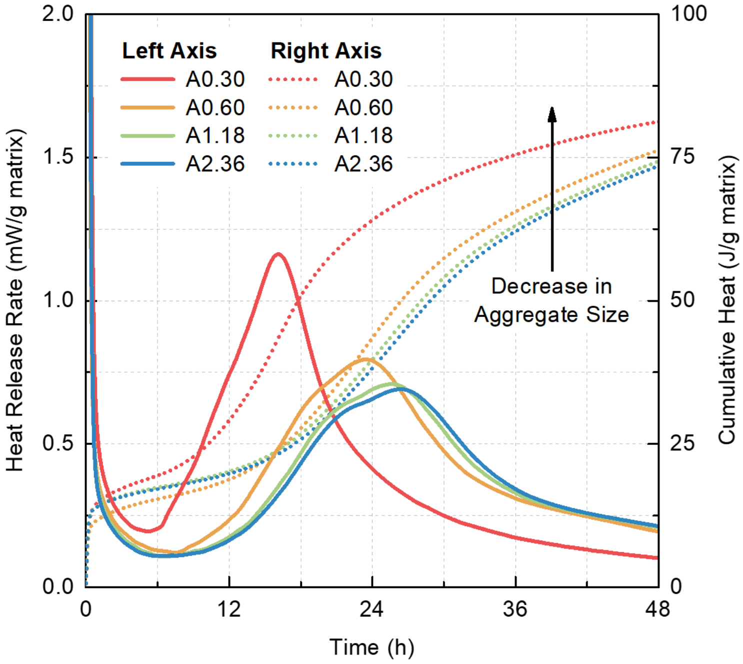

Fig. 7 Hydration heat of UHS-ECC matrices with different GPA size ranges. The solid and dotted lines represent the heat release rate and cumulative heat, respectively.

The accelerated heat release rate and increased cumulative heat could be observed when the GPA size was smaller than 0.30 mm (i.e., A0.30 in **Fig. 7**), because such GPA behaved more like powders than fine aggregates (see **Fig. 1** and **Fig. 2a**). For the descending part, the heat release rate of A2.36 (0.213 mW/g matrix), A1.18 (0.209 mW/g matrix), and A0.60 (0.194 mW/g matrix) became almost the same at the end of 48 h. However, for A0.30, a much smaller heat release rate was achieved at 48 h, indicating an accelerated hydration occurred in this mix. Therefore, GPA with small particle sizes (especially smaller than 0.30 mm) could significantly accelerate the hydration process of the UHS-ECC matrix, which may also influence the fiber/matrix bond strength.

4.2 Results of nanoindentation

Fig. 8 shows the optical microscope image and the corresponding contour mapping of the elastic modulus of the GPA/matrix interfacial region obtained from grid nanoindentation tests.

In **Fig. 8a**, the GPA side could be distinguished by a lighter color and comparatively loose structure with some remanent round FA particles, while the cementitious matrix was darker and denser with some angular unhydrated cement clinkers. Furthermore, from the contour mapping results (**Fig. 8b**), a higher average elastic modulus could be observed on the cementitious matrix side than that on the GPA side, which further demonstrated the flaw effect of GPA in the ultra-high-strength matrix. In details, most of the red patterns in the cementitious matrix represented unhydrated cement clinkers in the dense UHS-ECC matrix with an ultra-low water-to-binder ratio. On the other hand, only several light red areas could be observed on the GPA side (i.e., X = 10 μm, Y = 0; X = 30 μm, Y = 10 μm; and X = 80 μm, Y = 20 μm in **Fig. 8b**), which represented some remanent unreacted FA particles.

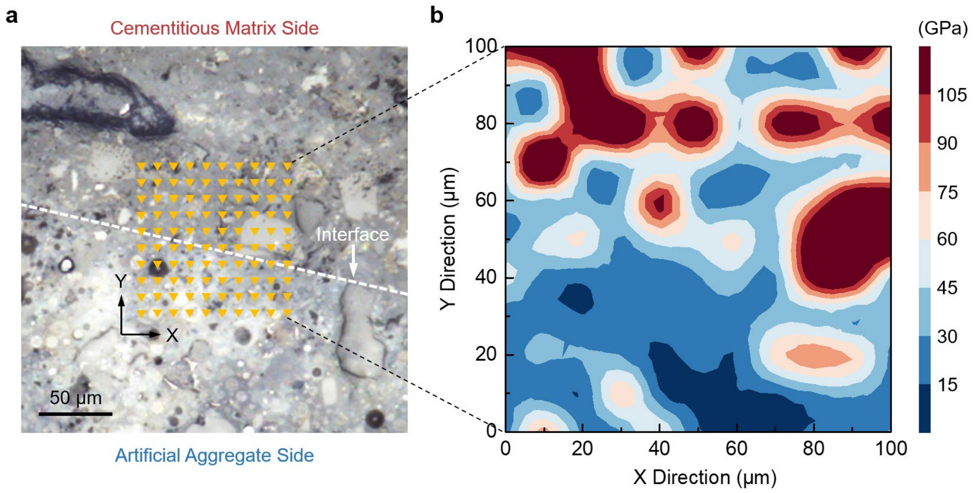

Fig. 8 Results of nanoindentation: (a) Optical microscope image of the GPA/matrix interfacial region (each triangle represents one indent), and (b) contour mapping of elastic moduli.

In order to quantitively analyze the different phases and products, statistical deconvolution was conducted on both sides of the GPA/matrix interface using Gauss Mixture Model, and the results are shown in **Fig. 9**. On the GPA side, as the GGBS/FA ratio was equal to 0.25 and almost no remanent GGBS particles were observed, three phases could be identified including unreacted FA, C-A-S-H, and N-(C)-A-S-H gels [75]. On the matrix side, main phases were identified as the cement clinker, calcium hydroxide (CH), and C-S-H in the sequence from the highest to the lowest elastic modulus [76]. Furthermore, the C-S-H gels can be divided into low-density (LD) C-S-H (elastic modulus < 27.5 GPa), high-density (HD) C-S-H (elastic modulus 27.5–33.3 GPa), and ultra-high-density (UHD) C-S-H (elastic modulus > 33.3 GPa) according to the nanogranular packing results obtained by Vandamme et al. [77].

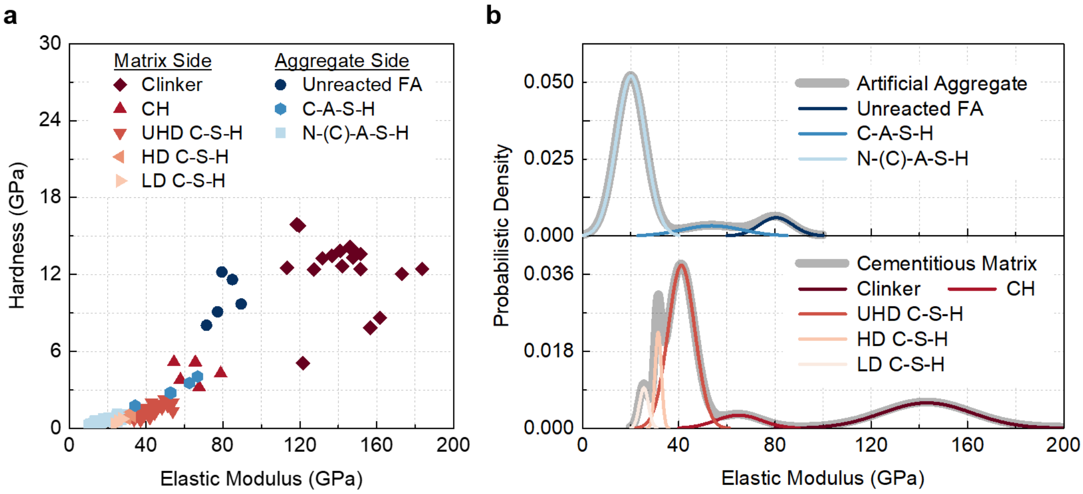

Fig. 9 (a) Cluster relationship of elastic modulus *vs.* hardness. The red and blue points represent the results on the matrix and GPA sides, respectively. (b) Distributions of the elastic moduli of GPA (the upper window) and cementitious matrix (the lower window). The gray line represents the overall distribution of the elastic moduli.

As presented in **Fig. 9a**, most indentation points on the GPA side were N-(C)-A-S-H gels, indicating a comparatively complete reaction degree of the blended FA/GGBS system near the GPA/matrix interfacial region. In comparison, the major hydration products of the cementitious matrix were UHD C-S-H, which showed higher elastic modulus and hardness than the N-(C)-A-S-H on the GPA side. **Fig. 9b** presents the distributions of the elastic moduli of all the phases together with the overall distribution of each side (the gray line). It can be found that the overall distribution of the elastic moduli of the cementitious matrix was larger than that of GPA. Although C-A-S-H gels showed larger elastic moduli than most of the C-S-H products, the ratio of C-A-S-H on the GPA side was comparatively low and most products were N-(C)-A-S-H (because the GGBS/FA ratio was only 0.25 in GPA production). In summary, according to the nanoindentation results of the GPA/matrix interface area, the cementitious matrix was found to be much stronger than GPA, which further confirmed the role of GPA as flaws in the ultra-high-strength matrix.

5 Micromechanics and over-saturated cracking of GPA-based UHS-ECC

5.1 Flaw effect of GPA and cracking strength

5.1.1 X-CT results

X-CT analysis was conducted to gain an in-depth understanding of the flaw effect of the GPA with different sizes. **Fig. 10** shows the reconstructed three-dimensional (3D) X-CT images of cracked UHS-ECC. Here, the 3D X-CT results of a small cube with the dimension of 7 mm × 7 mm × 7 mm are presented for each mix for better visibility. From the reconstructed images, the internal cracks, initial flaws (i.e., pores), and GPA could be clearly differentiated. It is clear that the distribution of GPA became more uniform as the GPA size decreased.

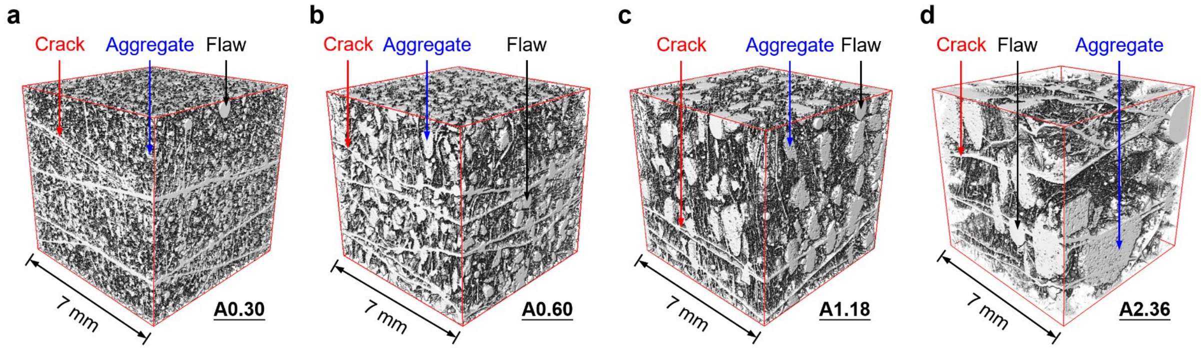

Fig. 10 Three-dimensional X-CT images of the GPA-based UHS-ECC: (a) A0.30, (b) A0.60, (c) A1.18, and (d) A2.36. The scanning result of a 7 mm × 7 mm × 7 mm cube was presented for each UHS-ECC mix.

5.1.2 Flaw effect of artificial geopolymer aggregates (GPA)

If one single or more cracks penetrated through an GPA in UHS-ECC matrix, it can be regarded as an active flaw, otherwise it is an inactive flaw. In **Fig. 11**, two-dimensional (2D) X-CT images were adopted for the flaw analysis based on the ImageJ software (resolution: 10.3 μm per pixel), because the flaw, aggregate, crack, and fibers in 2D presentation were easier to be distinguished than those in 3D presentation. Considering the stereology principles, the area fractions of GPA were the same in both 2D and 3D X-CT presentations [56, 78]. It is worth mentioning that the influence of GPA size on the distribution uniformity of PE fibers can also be observed in **Fig. 11**. Taking A2.36 for example (i.e., **Fig. 11d**), the clustered GPA at the lower-left corner disturbed the fiber distribution and consequently the fiber bridging effect.

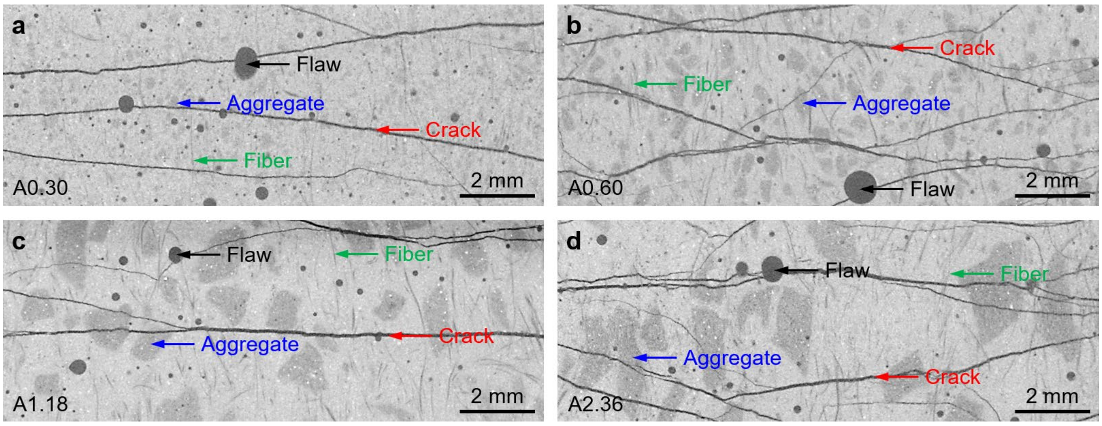

Fig. 11 Two-dimensional X-CT images of the cracked UHS-ECC: (a) A0.30, (b) A0.60, (c) A1.18, and (d) A2.36.

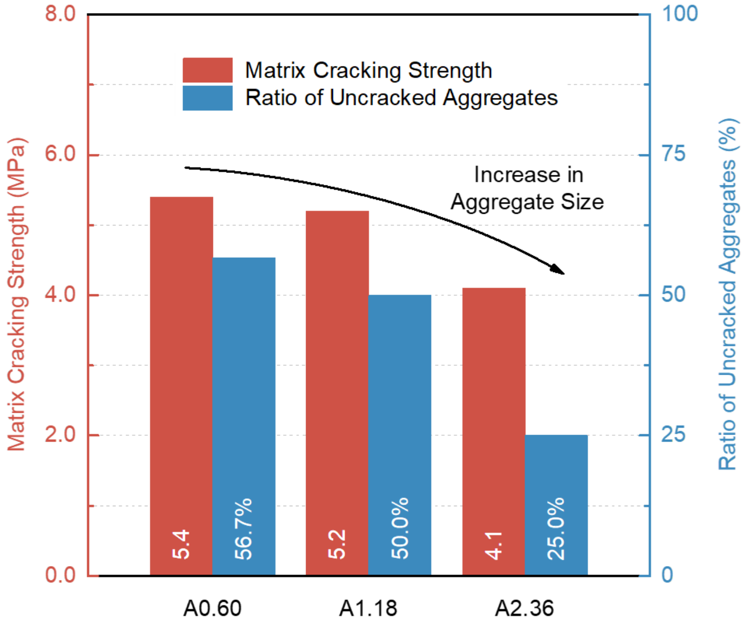

Fig. 12 Matrix cracking strength and ratio of uncracked GPA of UHS-ECC (A0.60, A1.18, and A2.36). The cracking strength of A0.30 was 6.7 MPa, but A0.30 was not adopted for the flaw analysis, because some GPA were too small to be distinguished.

Fig. 12 shows the matrix cracking strength of each mix together with the corresponding ratio of uncracked (or inactive) GPA obtained from **Fig. 11**. The ratio of uncracked GPA decreased from 56.7% to 25.0% with the increasing GPA size, and a similar trend was also observed in the matrix cracking strength. It should be pointed out that A0.30 was not adopted for the flaw analysis, because only part of GPA could be clearly observed in **Fig. 11a**, while the others were too small to be distinguished. The cracking strength of A0.30 was 6.7 MPa, which also followed the trend of cracking strength shown in **Fig. 12**. The above results were in accordance with the findings in normal-strength ECC with silica sand [79]. That is, the first cracking strength decreased with the increase of flaw size, and larger flaws could induce cracks in ECC more easily.

5.2 Micromechanical analysis

5.2.1 Fracture toughness K_m

The fracture toughness K_{m} of the UHS-ECC matrices with different GPA sizes was measured by three-point bending fracture tests (as described in *Section 2.4*). According to ASTM E399-19 [80], the matrix fracture toughness can be calculated as follows:

$$K_{\mathrm{m}}=\frac{P_{\mathrm{s}}S}{BW^{3/2}}\cdot 3\sqrt{\frac{a}{W}}\cdot\frac{1.99-\left(\frac{a}{W}\right)\left(1-\frac{a}{W}\right)\left[2.15-3.93\frac{a}{W}+2.7\left(\frac{a}{W}\right)^{2}\right]}{2\left(1+2\frac{a}{W}\right)\left(1-\frac{a}{W}\right)^{3/2}} \quad \textbf{(1)}$$

where P_{s} is the peak load obtained in the test, S, B, and W are the span, thickness, and width of the notched specimen, and a is the length of the crack. The calculated K_{m} values are listed in **Table 4**.

Table 4 Summary of micromechanical parameters of UHS-ECC.

Micromechanical Parameters		A0.30	A0.60	A1.18	A2.36
Strength Criterion	σ_{fc} (MPa)	6.7	5.4	5.2	4.1
	σ_0 (MPa)	20.7	19.0	16.8	12.3
	PSH_{Strength}	3.1	3.5	3.2	3.0
Energy Criterion	K_{m} (MPa·m$^{1/2}$)	0.955	0.908	0.977	0.924
	E_{m} (GPa)	32.3	31.1	31.6	30.8
	J_{tip} (J/m^2)	28.3	26.5	30.2	27.7
	J_{b}' (J/m^2)	3445	3447	3622	2594
	PSH_{Energy}	121.9	130.1	119.8	93.7

5.2.2 Fiber-bridging stress

Fig. 13a–d shows the fiber-bridging stress *vs.* crack opening relations of A0.30, A0.60, A1.18, and A2.36 obtained from single-crack tensile tests (two samples for each group exhibited almost the identical results). The average curve of each group is also plotted in **Fig. 13a–d**, and the comparison of the average results can be found in **Fig. 13e**. The maximum fiber-bridging stress (σ_0) decreased with the increasing GPA size. As shown in **Fig. 11**, the existence of large-size GPA influenced the fiber distribution, leading to the lowered fiber-bridging force.

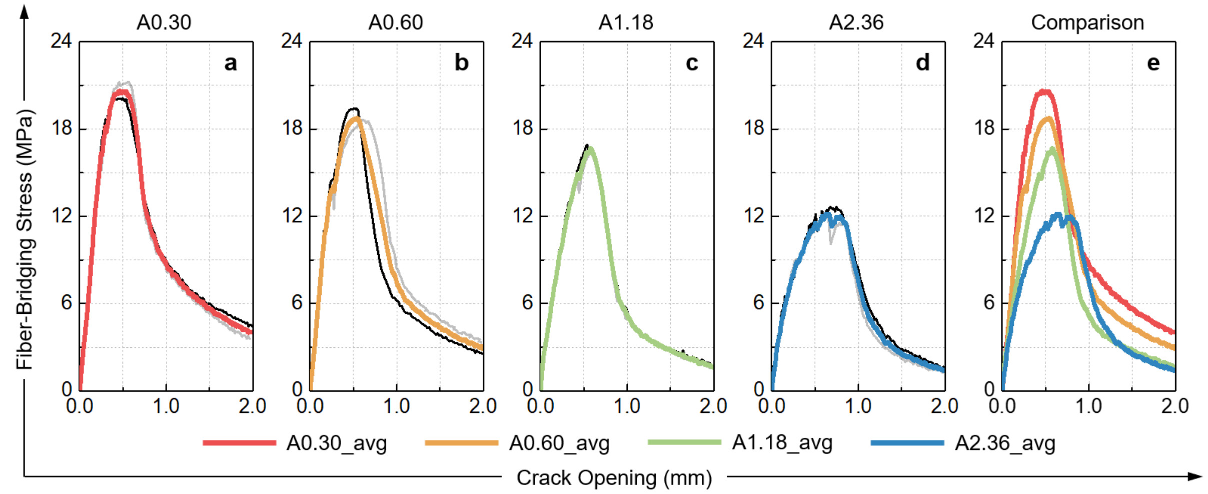

Fig. 13 Fiber-bridging stress *vs.* crack opening curves of UHS-ECC obtained from single-crack tensile tests. The average curves of all the groups are also plotted and compared.

5.2.3 Strength and energy criteria

The micromechanics theory is important for the design and strain-hardening ability of ECC materials [81, 82, 83]. According to the micromechanical design principle of strain-hardening cement-based materials [84], both the strength and energy criteria need to be satisfied. For the strength criterion, the maximum fiber-bridging stress σ_0 should be no less than the first cracking stress of matrix σ_{fc}:

$$\sigma_0 \geq \sigma_{fc} \tag{2}$$

where σ_0 and σ_{fc} can be obtained from the results of single-crack tensile tests and direct tensile tests, respectively. For the energy criterion, the complementary energy J_b' in **Fig. 14** should be no less than the crack tip toughness J_{tip}:

$$J_b' \equiv \sigma_0 \delta_0 - \int_0^{\delta_0} \sigma(\delta)\, d\delta \geq J_{tip} = K_{tip}^2 \left(1 - \nu^2\right) / E_c \cong K_m^2 / E_m \tag{3}$$

where K_{tip} is the fracture toughness of the crack tip, ν is the Poisson's ratio of the composite, E_c

is the elastic modulus of the composite, and E_m is the elastic modulus of the ECC matrix. Here, the crack opening displacement δ_0 corresponding to σ_0 can be obtained from single-crack tensile tests. The E_m values measured from the elastic modulus tests have been listed in **Table 4**.

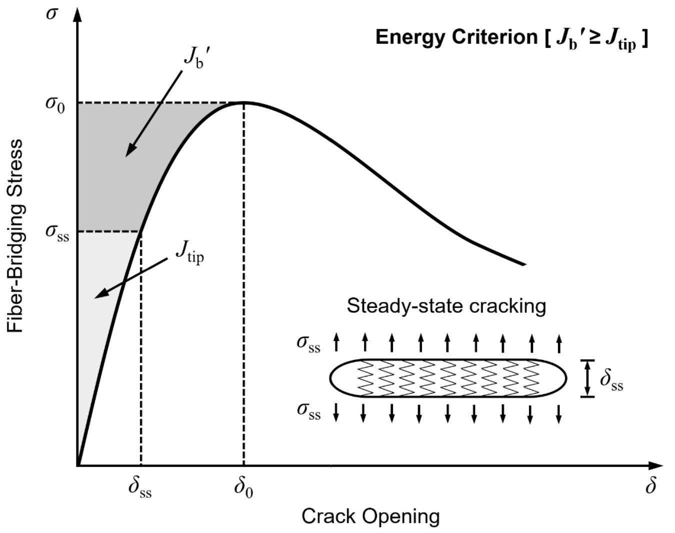

Fig. 14 Schematic diagram of energy criteria for strain-hardening cement-based materials (Adapted from Ref. [1]).

Based on the above two criteria, pseudo-strain-hardening (*PSH*) indices can be defined as follows [85, 86]:

$$PSH_{Strength} = \sigma_0 / \sigma_{fc} \tag{4}$$

$$PSH_{Energy} = J_b' / J_{tip} \tag{5}$$

where the calculated $PSH_{Strength}$ and PSH_{Energy} indices as well as the corresponding micromechanical parameters of UHS-ECC (i.e., σ_{fc}, σ_0, J_{tip}, and J_b') are listed in **Table 4**. It can be seen that the two criteria were satisfied for all the UHS-ECC mixes.

Since a strong relation exists between *PSH* indices and tensile strain capacity, they are plotted together in **Fig. 15**. In general, the variations of $PSH_{Strength}$ and PSH_{Energy} indices showed the similar trend with that of the tensile strain capacity. For example, A0.60 with the highest tensile strain capacity (i.e., 8.2%) showed the highest $PSH_{Strength}$ and PSH_{Energy} index values. It also indicated that the use of GPA with the particle size of 0.30–0.60 mm could achieve the most significant tensile strain-hardening in UHS-ECC materials.

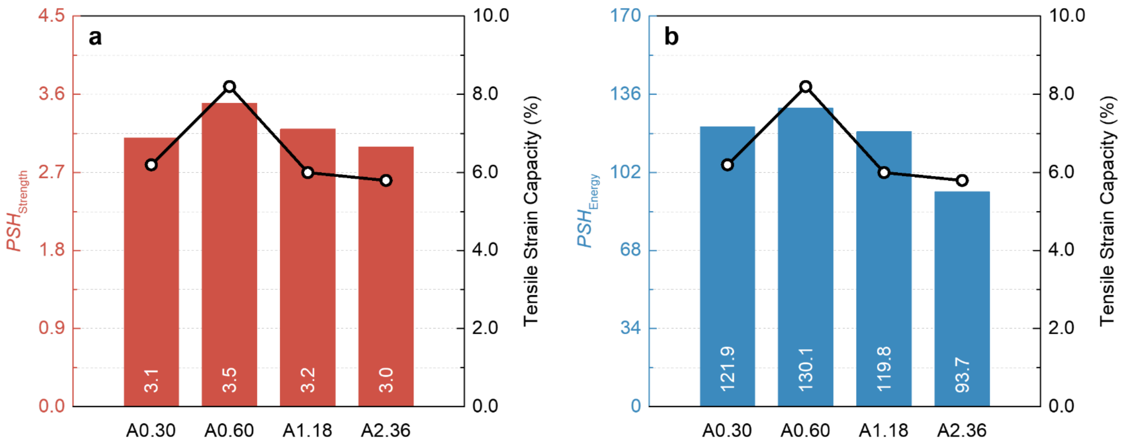

Fig. 15 Comparison of *PSH* indices and tensile strain capacity of UHS-ECC: (a) $PSH_{Strength}$ *vs.* tensile strain capacity, and (b) PSH_{Energy} *vs.* tensile strain capacity. The bar chart represents the *PSH* index and the line chart represents the tensile strain capacity.

5.3 Tensile cracking behavior

5.3.1 Theoretical crack spacing

Average crack spacing is an important parameter for evaluating the multiple cracking behavior of strain-hardening cement-based materials. Generally speaking, a more saturated multiple cracking means a larger crack number with a smaller average crack spacing. According to the micromechanics of ECC, the theoretical crack spacing considering the snubbing effect can be given as follows [87].

$$x_d = \frac{L_f - \sqrt{L_f^2 - 2\pi L_f \psi x}}{2} \tag{6}$$

$$\psi = \frac{1+f^2}{e^{f\pi/2} - f} \tag{7}$$

$$x = \frac{\left(1-V_f\right)\sigma_m d_f}{4\tau_0 V_f} \tag{8}$$

where x_d is the theoretical crack spacing for the two-dimensional (2D) random fiber distribution condition; L_f, d_f, and V_f are the length, diameter, and volume fraction of PE fibers used in the composites, which are equal to 18 mm, 0.024 mm, and 2%, respectively; f is the snubbing coefficient, which was found to be 0.59 for PE fibers in the ultra-high-strength matrix [88]; σ_m

is the matrix cracking strength, which can take the value of σ_{fc} from **Table 4**; and τ_0 is the interfacial frictional bond of fiber. For the tensile specimens in this study, the UHS-ECC was cast into the dumbbell mold (13-mm thick) in two equal layers and the 18-mm PE fiber was much larger than the layer thickness. Thus, the 2D fiber distribution was assumed.

The interfacial frictional bond of PE fiber τ_0 was not directly measured in this study, but it could be estimated based on the maximum fiber-bridging stress in **Fig. 13**. For fiber-reinforced cementitious composites, the relationship between the fiber interfacial frictional bond τ_0 and the maximum fiber-bridging stress σ_0 in the 2D fiber distribution can be expressed as follows [89, 90].

$$\sigma_0 = \frac{2}{\pi} g \tau_0 V_f \left(\frac{L_f}{d_f} \right) \qquad \textbf{(9)}$$

$$g = \frac{2}{4+f^2}\left(1+e^{\pi f/2}\right) \qquad \textbf{(10)}$$

where g is the snubbing factor. Here, the values of τ_0 can be obtained by introducing σ_0 (**Table 4**) into **Eq. (9)** and **Eq. (10)**. The calculated τ_0 values of A0.30, A0.60, A1.18, and A2.36 were 1.31 MPa, 1.23 MPa, 1.08 MPa, and 0.79 MPa, respectively. It should be pointed out that compared with the τ_0 obtained from a single fiber test, the calculated τ_0 (as an equivalent value) was more suitable for estimating the crack spacing influenced by both matrix properties and GPA size. Based on **Eqs. (6–10)**, the theoretical crack spacing x_d for A0.30, A0.60, A1.18 and A2.36 were calculated as 1.8 mm, 1.5 mm, 1.7 mm, and 1.8 mm, respectively.

5.3.2 Tensile over-saturated cracking

In order to better indicate the pseudo strain-hardening potential from the aspect of crack spacing, the definition of *PSH* intensity is given as follows [91]:

$$PSH\ Intensity = x_d^t / x_d \qquad \textbf{(11)}$$

where x^t_d is the average crack spacing obtained from direct tensile test, whose values were 1.2 mm, 1.1 mm, 1.9 mm, and 1.8 mm for A0.30, A0.60, A1.18 and A2.36, respectively, as presented in **Fig. 16**.

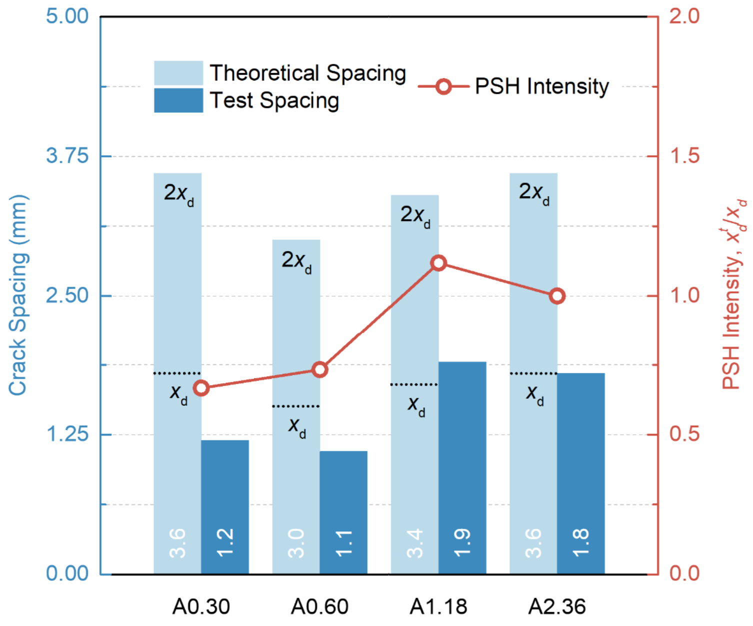

Fig. 16 Crack spacing and *PSH* intensity of UHS-ECC with different GPA sizes. The bar chart represents the crack spacing and the line chart represents the *PSH* intensity.

According to the previous study [91], saturated multiple cracking of ECC can be achieved when the x^t_d is between x_d and $2x_d$ (i.e., $1 \leq PSH$ intensity ≤ 2). Obviously, this condition was satisfied for A1.18 and A2.36 (**Fig. 16**), whose *PSH* intensities were equal to 1.12 and 1.00, respectively. However, for A0.30 and A0.60 in **Fig. 16**, the average crack spacing x^t_d was found significantly smaller than the theoretical crack spacing limit (i.e., x_d), leading to the *PSH* intensities significantly smaller than 1 (i.e., 0.67 for A0.30, and 0.73 for A0.60). The authors suggest that this phenomenon (i.e., average tensile crack spacing x^t_d smaller than the theoretical limit x_d) could be named as over-saturated cracking. In the next section, based on the tensile stress–strain curves and crack evolution processes, the mechanism of the over-saturated cracking in GPA-based UHS-ECC will be further analyzed and discussed in detail.

6 Understanding of the mechanism of over-saturated cracking

6.1 Crack numbers at different strain levels

In this section, one typical tensile sample was selected for each group (i.e., A0.30_1, A0.60_1, A1.18_1, and A2.36_1 in **Fig. 5**) to analyze the cracking behaviors of the GPA-based UHS-ECC. For each selected sample, the tensile strains ranging from 0.2% to the ultimate strain were equally divided into 11 strain levels. The crack numbers within the measured gauge length (i.e., L_g = 80 mm in **Fig. 3a**) are plotted in **Fig. 17**, which were obtained from the digital photographs at all the selected strain levels. It is noted that these crack numbers were counted alone the central line of the specimen in the digital photographs.

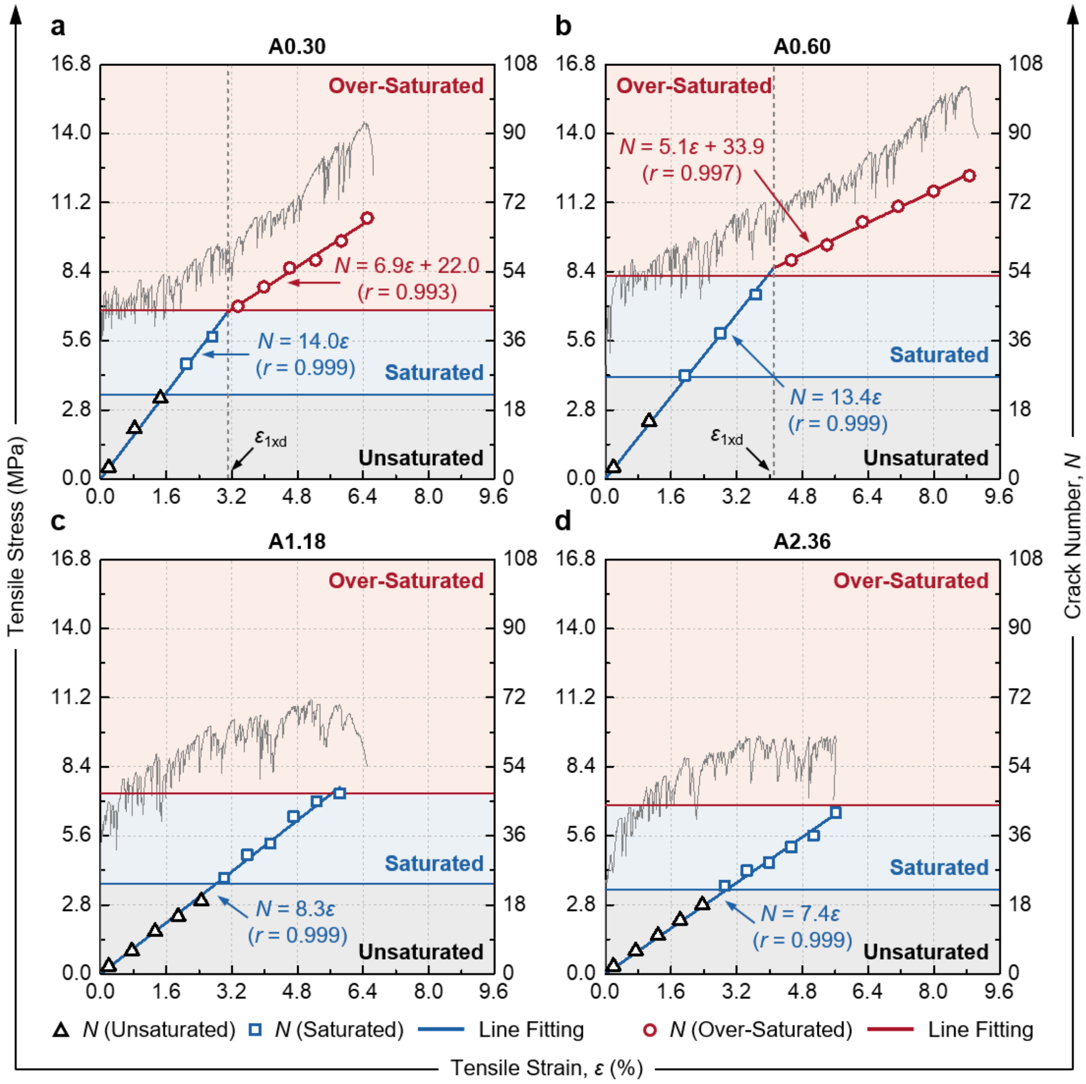

Fig. 17 Crack numbers of the GPA-based UHS-ECC at different tensile strain levels: (a) A0.30, (b) A0.60, (c) A1.18 and (d) A2.36. **Eq. (12)** was used for the curve fitting. The unsaturated, saturated, and over-saturated cracking are determined by the theoretical crack spacing shown in **Fig. 16**.

In **Fig. 17**, the thresholds of the unsaturated, saturated, and over-saturated cracking conditions are determined by the theoretical crack spacing (x_d in **Fig. 16**) and the gauge length L_g. That is, when the actual crack number N is smaller than $L_g/2x_d$, between $L_g/2x_d$ and L_g/x_d, and larger than L_g/x_d, the corresponding cracking conditions are classified as the unsaturated, saturated, and over-saturated cracking, respectively.

For all the groups in **Fig. 17**, the crack numbers increased linearly as the tensile strain increased during both the unsaturated and saturated cracking stages (i.e., $x^t_d \geq x_d$), which indicated a steady-state multiple cracking of the GPA-based UHS-ECC. It is worth mentioning that for A0.30 and A0.60, an inflection point can be clearly observed near the threshold between the saturated and over-saturated cracking stages (i.e., $x^t_d = x_d$). After the inflection point, the growth of the crack number was slower, but a linear N–ε relation could still be observed under the over-saturated cracking condition. However, this phenomenon was not observed in A1.18 and A2.36 (i.e., **Fig. 17c–d**), and their crack numbers at the ultimate tensile strain could not exceed the theoretical limit (i.e., L_g/x_d). Based on the results presented in **Fig. 17**, a bilinear fitting was applied to describe the double-stage evolution of the crack number of A0.30 and A0.60 (i.e., **Fig. 17a–b**), while a linear fitting was used for A1.18 and A2.36 (i.e., **Fig. 17c–d**). The fitting results showed good agreement with the experimental outcomes. It should be pointed out that $\varepsilon_{1\text{xd}}$ in **Fig. 17a–b** was determined by the intersection of the two fitted lines, and the crack number at $\varepsilon_{1\text{xd}}$ (i.e., $N_{1\text{xd}}$) was found to be close to the theoretical value (i.e., L_g/x_d).

6.2 Crack widths s at different strain levels

In the previous section, different cracking conditions were defined based on the theoretical crack spacing (i.e., unsaturated, saturated, and over-saturated cracking conditions). As the crack width control is important for the durability of concrete infrastructure [29], it is significant to understand the crack width evolutions of UHS-ECC at different cracking conditions.

For each specimen in **Fig. 17**, the crack widths and numbers at different strain levels could be obtained from the digital photographs according to the method in Ref. [4]. **Fig. 18** presents the fitted crack width distributions of UHS-ECC (using Weibull distribution [4]) at different crack saturation conditions. It is noted that the crack distributions with similar *PSH* intensities (i.e., x^t_d/x_d) were plotted for all the UHS-ECC mixes. **Fig. 18a** and **Fig. 18b** show the crack distributions under the unsaturated and saturated cracking conditions, respectively. In **Fig. 18c**, the crack distributions at the ultimate stage of UHS-ECC are presented (over-saturated cracking for A0.30 and A0.60, and saturated cracking for A1.18 and A2.36).

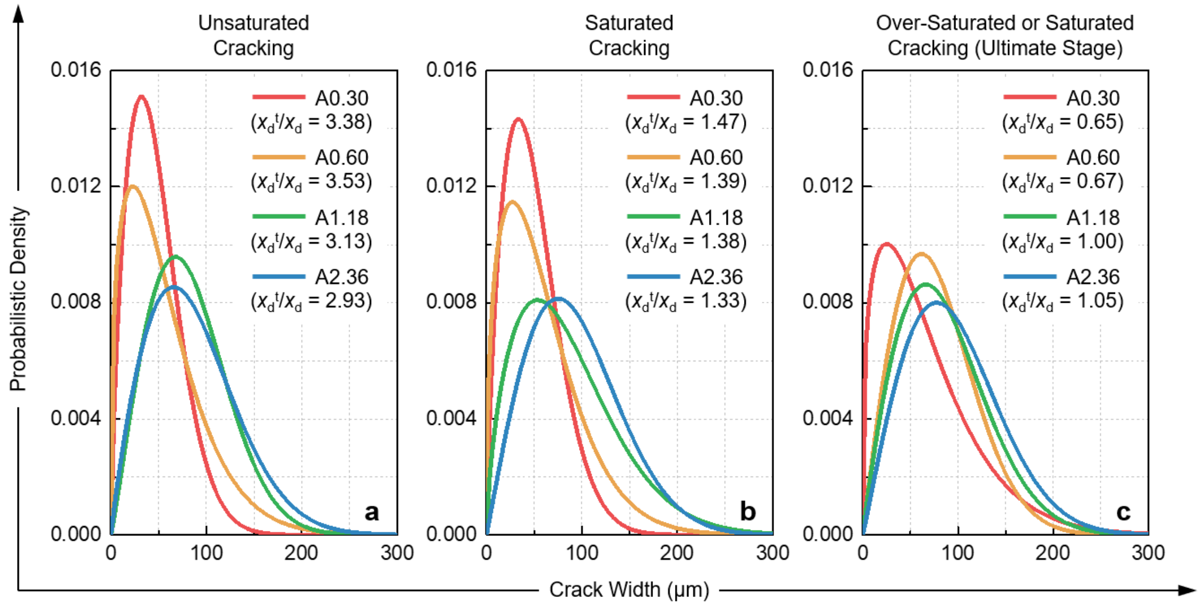

Fig. 18 Crack width distributions of UHS-ECC at different crack saturation conditions: (a) Unsaturated cracking, (b) saturated cracking, and (c) ultimate failure (over-saturated cracking for A0.30 and A0.60, and saturated cracking for A1.18 and A2.36).

By comparing the crack distribution curves of different mixes, A0.30 and A0.60 showed smaller crack widths than A1.18 and A2.36 at the similar *PSH* intensities. In addition, comparing **Fig. 18a** and **Fig. 18b,** the shapes of the distribution curves of all the mixes did not change significantly, indicating a steady-state crack evolution of UHS-ECC under both unsaturated and saturated cracking conditions. However, at the ultimate stage, the shapes of the distribution curves of A0.30 and A0.60 became much flatter and wider, indicating that the growth of the crack width became faster at the over-saturated cracking condition. This phenomenon will be further demonstrated in the following sections.

Fig. 19 presents the average crack widths of UHS-ECC at different strain levels. Here, the strain levels are the same with those used in **Fig. 17**. A bilinear fitting can also be adopted to describe the double-stage evolution of the average crack width (**Fig. 19a–b**), while a linear fitting can be used for A1.18 and A2.36 in **Fig. 19c–d**. The bilinear and linear fitting results showed good agreements with the *w*–*ε* relations of the GPA-based UHS-ECC. It can be seen in **Fig. 19a–b** that the growth of crack width during the over-saturated cracking stage was faster than that during the first stage (i.e., unsaturated and saturated cracking).

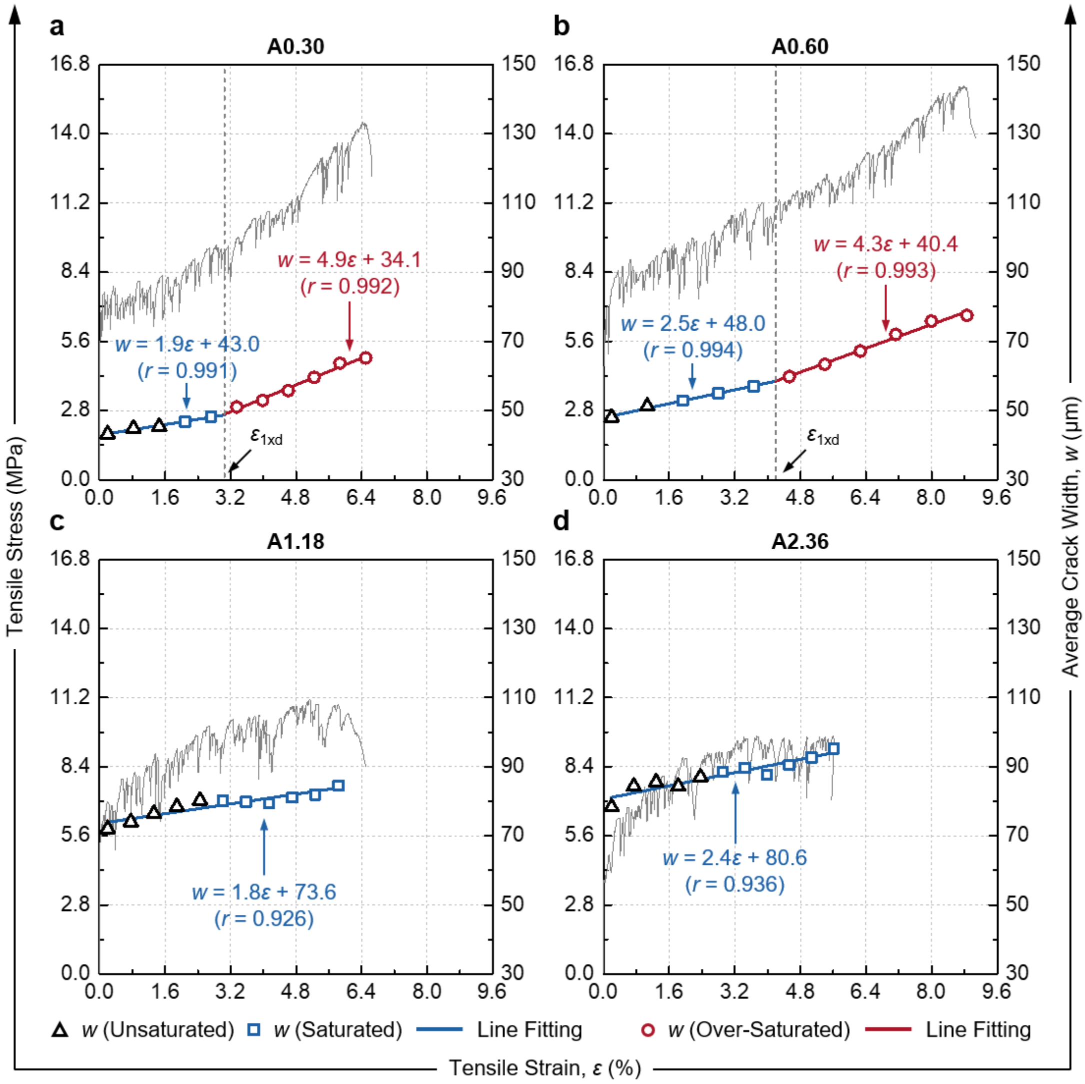

Fig. 19 The average crack widths of UHS-ECC at different strain levels: (a) A0.30, (b) A0.60, (c) A1.18 and (d) A2.36.

6.3 Comparison of cracking behavior

Considering that the crack width is critical for the durability and self-healing ability of cement-based materials [2], **Fig. 20** shows the variations of average crack widths and crack numbers at different strain levels of the GPA-based UHS-ECC. For A0.30 and A0.60, the growth of the crack width became faster after the inflection points, while that of the crack number became slower. According to ACI 318-14 [92], the allowable crack width is usually within 0.2–0.3 mm. From **Fig. 20**, the average crack widths of all the mixes met the requirement of ACI 318-14. For the same tensile strain level, as the particle size of GPA decreased, the crack number increased but the average crack widths decreased, indicating the better durability of

UHS-ECC with smaller GPA.

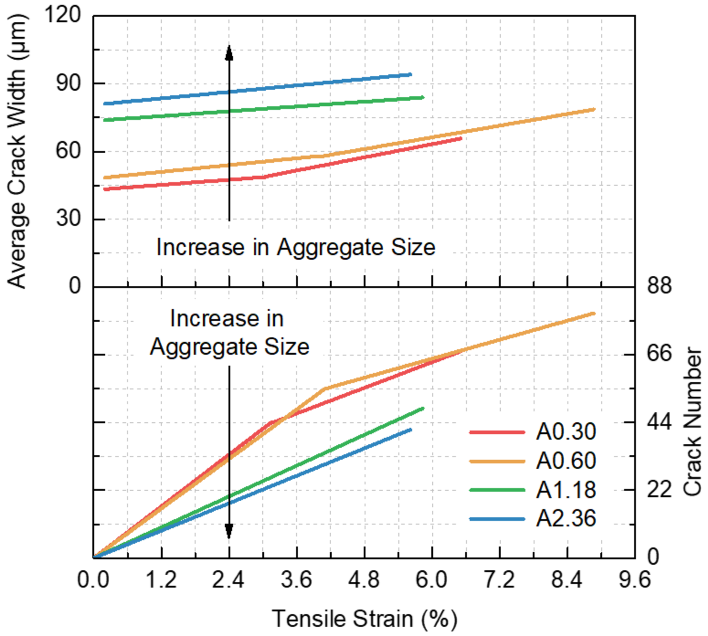

Fig. 20 Variations of average crack widths and crack numbers at different tensile strain levels of the GPA-based UHS-ECC.

6.4 Crack patterns at selected strain levels

To better understand the crack evolution, the crack patterns of A0.30 and A0.60 at four selected strain levels are presented in **Fig. 21**. The first and second strain levels were $0.49\varepsilon_{1xd}$ (unsaturated cracking) and ε_{1xd} (saturated cracking), respectively. The third strain level was $0.5(\varepsilon_{1xd} + \varepsilon_u)$, and the last strain level was the ultimate tensile strain (ε_u). It is noted that the third and last strain levels belonged to the over-saturated cracking condition.

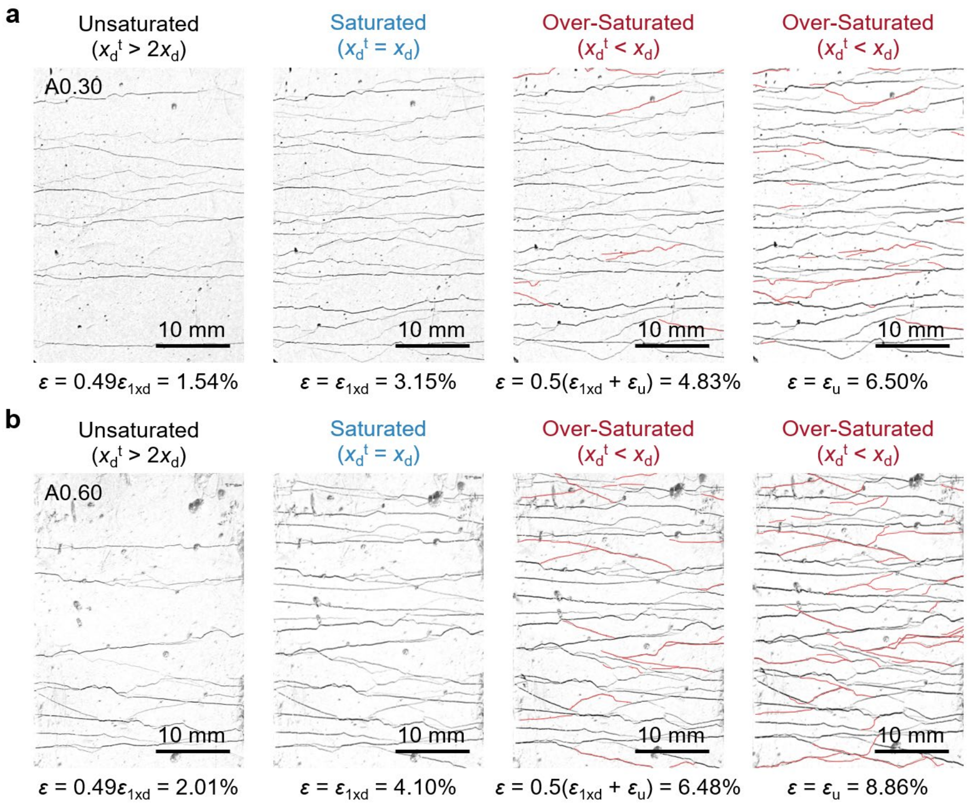

Fig. 21 Crack patterns of UHS-ECC at four selected strain levels: (a) A0.30 and (b) A0.60. The cracks appeared after ε_{1xd} (i.e., $x^t_d = x_d$) were marked in red.

In **Fig. 21**, the parallel steady-state cracks could be observed at the unsaturated and saturated cracking stages, and the crack number increased with the increasing tensile strain. At the over-saturated cracking condition, the growth of crack number became much slower (see also **Fig. 17a–b**) and the widths of the existing cracks became larger (see the cracks turning darker in **Fig. 21**). Here, the new cracks generated after ε_{1xd} (i.e., $x^t_d = x_d$) were marked in red. It can be observed that unlike the parallel cracks observed in the unsaturated and saturated cracking conditions, most of the over-saturated cracks were locally generated. It is inferred that such cracks were related to the existence of the weak GPA (or initial flaws) between two parallel cracks. Under tensile loading, the local cracks initiated and propagated from the GPA (or initial flaws) and finally linked the existing parallel steady-state cracks, which further reduced the tested crack spacing value. More detailed discussions on the mechanism of the over-saturated cracking will be presented in the following section.

6.5 Mechanism of over-saturated cracking

Based on the aforementioned experimental findings, the over-saturated cracking of ECC materials can be defined as the cracking condition where the average tensile crack spacing (x^t_d) is smaller than the theoretical limit (x_d). In addition, the over-saturated cracking is accompanied with a double-stage crack evolution. **Fig. 22a** summarizes the variations of tensile stress (σ), crack width (w), crack number (N), and average crack spacing (x^t_d) at different tensile strain (ε) of ECC material with over-saturated cracking. In **Fig. 22a**, σ_{fc} and ε_{fc} are the cracking stress and strain, respectively; σ_{2xd} and ε_{2xd} are the stress and strain at $x^t_d = 2x_d$, respectively; σ_{1xd} and ε_{1xd} are the stress and strain at $x^t_d = x_d$, respectively; and σ_{u} and ε_{u} are the stress and strain at the ultimate stage, respectively. The schematic diagrams of the crack patterns at different stages are presented in **Fig. 22b**.

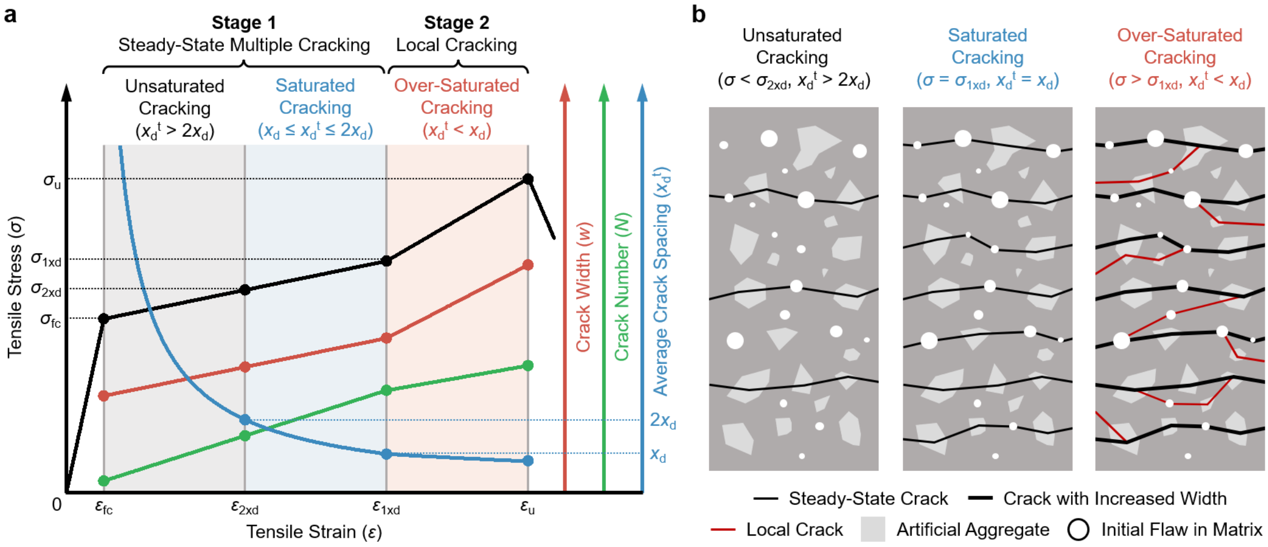

Fig. 22 Schematic diagram of the mechanism of over-saturated cracking and double-stage crack evolution: (a) Variations of tensile stress σ, crack width w, crack number N, and average crack spacing x^t_d at different tensile strain ε; and (b) crack patterns at unsaturated, saturated, and over-saturated cracking conditions.

At the first stage of the crack evolution (i.e., Stage 1 in **Fig. 22a**), as the tensile strain increases from zero to ε_{1xd}, the steady-state multiple cracking occurs (mainly parallel cracks in **Fig. 22b**) and the crack number increases from zero linearly. It is noted that the cracking behaviors of the UHS-ECC with different GPA sizes are similar at this stage. The addition of

GPA lowers the matrix cracking strength and fracture toughness, and hence more cracks will be generated during the steady-state multiple cracking. For UHS-ECC in tension, cracks firstly emerge in the sections with lower cracking strength, and then generate in the sections with higher cracking strength. Thus, the tensile stress gradually becomes higher. Once the fiber-bridging stress is lower than the stress of the next crack initiation, the multiple cracking process may terminate. It should be remembered that the larger GPA size will cause the non-uniform distribution of fibers and result in a lower fiber-bridging force (see **Fig. 13**). Thus, compared to A0.30 and A0.60, the terminations of the multiple cracking process of A1.18 and A2.36 are earlier with $\sigma_{\mathrm{u}} < \sigma_{\mathrm{1xd}}$ and $x^t_d > x_d$, leading to the phenomenon of single-stage crack evolution. For A0.30 and A0.60 with larger fiber-bridging force, the cracking process can continue after $x^t_d = x_d$.

According to the micromechanical theory of ECC, x_d calculated by **Eqs. (6–8)** should be the theoretical minimum crack spacing. If the tensile stress continues increasing after the inflection point ($x^t_d = x_d$), the crack width will increase faster but the crack number remains unchanged. Theoretically, the strain increment after the inflection point ($x^t_d = x_d$) is only related to the crack opening. It should be pointed out that the theoretical limit of crack spacing [i.e., **Eqs. (6–8)**] is calculated based on the assumption that the ECC matrix is uniform. However, owing to the existence of GPA and initial flaws, the matrix between two parallel cracks is in fact not uniform for the GPA-based UHS-ECC. Thus, after the inflection point ($x^t_d = x_d$), the new local cracks form and link the existing cracks with the increasing tensile stress, which results in the over-saturated cracking (**Fig. 22b**). At the second stage of A0.30 and A0.60 (i.e., Stage 2 in **Fig. 22a**), the crack number keeps increasing (contributed from local cracking) and the widths of the existing cracks also become larger (similar to the theoretical condition mentioned above). That is, the strain increment in the over-saturated cracking condition is related to both crack opening and local cracking of the GPA-based UHS-ECC.

Based on the aforementioned mechanisms of over-saturated cracking, it can be concluded that the lower matrix cracking strength (to minimize the spacing of steady-state cracks) and the higher fiber-bridging force (to ensure $\sigma_{\mathrm{u}} > \sigma_{\mathrm{1xd}}$) are desirable for realizing the over-saturated cracking in ECC materials. For A0.30 and A0.60, the addition of GPA lowered the cracking strength and the small-size GPA also minimized their influence on the fiber distribution (i.e., ensured adequate fiber-bridging force). Thus, the over-saturated cracking occurred in these two mixes.

Actually, understanding the mechanisms behind the over-saturated cracking is meaningful for achieving ultra-high tensile ductility in ECC materials, especially for HS/UHS-ECC, because it remains challenging to achieve ultra-high compressive strength (e.g., > 150 MPa) and ultra-high tensile ductility (e.g., > 8%) simultaneously in cement-based materials. In addition, the findings of this study indicate that GPA with the size of 0.30–0.60 mm could be an effective material modifier for enhancing the tensile performance of UHS-ECC. On the other hand, the double-stage crack evolution of ECC is also useful for the application in durable and resilience structural members. The first stage (i.e., steady-state multiple cracking stage in **Fig. 22a**) with comparatively small crack width is beneficial for enhancing the structural durability under service loadings (i.e., with low strain level). The second stage with high tensile strain level but larger crack width can be utilized to improve the resilience of structural members under extreme loading conditions (e.g., seismic and impact loadings). In such cases, the crack width control is less important but the ultimate tensile strain capacity is critical.

7 Conclusions

In this study, artificial geopolymer aggregates (GPA) with different sizes (i.e., < 0.30 mm, 0.30–0.60 mm, 0.60–1.18 mm, and 1.18–2.36 mm) were used to develop ultra-high-strength Engineered Cementitious Composites (UHS-ECC). A multi-scale investigation was conducted to understand the influence of GPA size on the properties of UHS-ECC. Notably, over-saturated cracking and double-stage crack evolution were observed in UHS-ECC with small GPA sizes (< 0.60 mm) and the mechanism behind was revealed. The main conclusions are as follows.

- GPA reacted with the cementitious matrix of UHS-ECC. The matrix with finer GPA generated higher hydration heat due to the larger specific surface area. From the nanoindentation results, a lower average elastic modulus was measured in the GPA side than that in the cementitious matrix side, which verified the flaw effect of GPA. In addition, the compressive strength of UHS-ECC gradually decreased with increasing GPA size.

Overall, ultra-high-strength was achieved for all the UHS-ECC mixes developed (147.4–165.6 MPa).

- In terms of tensile performance, UHS-ECC with fine silica sand generally showed higher tensile strength but lower tensile strain capacity compared to the mixes using GPA as fine aggregates. In addition, UHS-ECC with the GPA size of 0.30–0.60 mm showed the highest tensile strain capacity (8.2%), tensile strength (15.2 MPa), and strain energy density (858.5 kJ/m^3). UHS-ECC with larger GPA showed a lower first cracking strength. In addition, the larger GPA size influenced the uniform distribution of fibers, leading to a more localized cracking behavior.
- The fiber-bridging force of UHS-ECC decreased with the increasing GPA size. According to the micromechanical analysis, A0.60 showed the highest tensile strain-hardening potential, which is in accordance with the direct tensile results. Notably, the average crack spacing of UHS-ECC with GPA size < 0.60 mm was significantly smaller than the theoretical minimum crack spacing, which indicated the over-saturated cracking of these mixes.
- Double-stage crack evolution together with over-saturated cracking was observed in UHS-ECC with GPA < 0.60 mm. The first stage of the double-stage crack evolution was dominated by steady-state multiple cracking, and the second stage was dominated by local cracking. The over-saturated cracking at the second stage was mainly related to the local cracks initiated from the GPA (or initial flaws) between the parallel steady-state cracks.
- In summary, GPA with the size of 0.30–0.60 mm could be an effective modifier for improving the tensile performance of UHS-ECC. In addition, the lower matrix cracking strength and the higher fiber-bridging force are desirable for realizing over-saturated cracking, which is useful for achieving ultra-high tensile ductility in HS/UHS-ECC. The double-stage crack evolution of GPA-modified UHS-ECC is meaningful for enhancing the durability and resilience of structural members under service and extreme loadings.

For the GPA-based UHS-ECC in this study, the GPA size and matrix rheology may impact fiber dispersion and the composite properties. It is an important research topic for UHS-ECC with different GPA sizes, and more efforts are needed in the following work. It should be pointed out that the GPA technology was initially developed for waste treatment and recycling, which can reduce industrial waste landfills and also reduce natural aggregate consumption. However, the current GPA technology is still more complex compared to natural aggregates. Based on the mechanism revealed in this study, alternative aggregates with low mechanical strength (e.g., lightweight aggregates and other types of artificial aggregates) may also be used in HS/UHS-ECC to achieve over-saturated cracking, and more efforts are appreciated in this research area.

Acknowledgments

The authors would like to acknowledge the financial support received from NSFC/RGC Joint Research Scheme (N_PolyU542/20), and Research Centre for Resources Engineering towards Carbon Neutrality (No. BBC7). Ling-Yu Xu acknowledges the PhD studentship offered by The Hong Kong Polytechnic University. Bo-Tao Huang and Jian-Cong Lao would like to acknowledge the support by the Hong Kong Innovation and Technology Fund (Project Code: ITS/077/18FX) through the Research Talent Hub.

Declaration of competing interest

The authors declare that they have no known competing financial interests or personal relationships that could have appeared to influence the work reported in this paper.

CRediT Author Statement

LY Xu: Conceptualization, Investigation, Validation, Writing - Original Draft. **BT Huang**: Conceptualization, Methodology, Formal analysis, Visualization, Writing - Review & Editing. **JC Lao**: Investigation, Validation. **J Yao**: Formal analysis, Writing - Review & Editing. **VC Li**: Supervision, Writing - Review & Editing. **JG Dai**: Conceptualization, Funding Acquisition, Project administration, Supervision, Writing - Review & Editing.

References

1. Li, V. C. (2019). *Engineered Cementitious Composites (ECC) - Bendable Concrete for Sustainable and Resilient Infrastructure*. Verlag GmbH Germany: Springer, Berlin, Heidelberg.

2. Yu, J., Yao, J., Lin, X., Li, H., Lam, J. Y., Leung, C. K., Sham, I. M. L. & Shih, K. (2018). Tensile performance of sustainable strain-hardening cementitious composites with hybrid PVA and recycled PET fibers. *Cement and Concrete Research*, 107, 110-123.

3. Li, V. C., Bos, F. P., Yu, K., McGee, W., Ng, T. Y., Figueiredo, S. C., Nefs, K., Mechtcherine, V., Nerella, V. N., Pan, J., van Zijl, G. P.A.G., & Kruger, P. J. (2020). On the emergence of 3D printable engineered, strain hardening cementitious composites (ECC/SHCC). *Cement and Concrete Research*, 132, 106038.

4. Huang, B. T., Wu, J. Q., Yu, J., Dai, J. G., Leung, C. K., & Li, V. C. (2021). Seawater sea-sand engineered/strain-hardening cementitious composites (ECC/SHCC): Assessment and modeling of crack characteristics. *Cement and Concrete Research*, 140, 106292.

5. Yu, K., Ding, Y., & Zhang, Y. X. (2020). Size effects on tensile properties and compressive strength of engineered cementitious composites. *Cement and Concrete Composites*, 113, 103691.

6. Khan, M., Cao, M., Xie, C., & Ali, M. (2022). Effectiveness of hybrid steel-basalt fiber reinforced concrete under compression. *Case Studies in Construction Materials*, 16, e00941.

7. Khan, M., Cao, M., Chu, S. H., & Ali, M. (2022). Properties of hybrid steel-basalt fiber reinforced concrete exposed to different surrounding conditions. *Construction and Building Materials*, 322, 126340.

8. Yoo, D. Y., & Banthia, N. (2016). Mechanical properties of ultra-high-performance fiber-reinforced concrete: A review. *Cement and Concrete Composites*, 73, 267-280.

9. Yoo, D. Y., & Banthia, N. (2019). Impact resistance of fiber-reinforced concrete–A review. *Cement and Concrete Composites*, 104, 103389.

10. Zhou, J., Pan, J., & Leung, C. K. (2015). Mechanical behavior of fiber-reinforced engineered cementitious composites in uniaxial compression. *Journal of Materials in Civil Engineering*, 27(1), 04014111.

11. Yin, X., Li, Q., Xu, X., Chen, B., Guo, K., & Xu, S. (2023). Investigation of continuous surface cap model (CSCM) for numerical simulation of strain-hardening fibre-reinforced cementitious composites against low-velocity impacts. Composite Structures, 304, 116424.

12. Li, S., Chan, T. M., & Young, B. (2022). Compressive behavior and analysis-oriented model of FRP-confined engineered cementitious composite columns. *Engineering Structures*, 270, 114869.

13. Hou, W., Lin, G., Li, X., Zheng, P., & Guo, Z. (2020). Compressive behavior of steel spiral confined engineered cementitious composites in circular columns. *Advances in Structural Engineering*, 23(14), 3075-3088.

14. Rokugo, K., Kanda, T., Yokota, H., & Sakata, N. (2009). Applications and recommendations of high performance fiber reinforced cement composites with multiple fine cracking (HPFRCC) in Japan. *Materials and Structures*, 42(9), 1197.

15. Huang, B. T., Li, Q. H., Xu, S. L., & Zhou, B. (2019). Strengthening of reinforced concrete structure using sprayable fiber-reinforced cementitious composites with high ductility. *Composite Structures*, 220,

940-952.

16. Ranade, R., Li, V. C., Stults, M. D., Heard, W. F., & Rushing, T. S. (2013). Composite properties of high-strength, high-ductility concrete. *ACI Materials Journal*, 110(4), 413-422.

17. Curosu, I., Liebscher, M., Mechtcherine, V., Bellmann, C., & Michel, S. (2017). Tensile behavior of high-strength strain-hardening cement-based composites (HS-SHCC) made with high-performance polyethylene, aramid and PBO fibers. *Cement and Concrete Research*, 98, 71-81.

18. He, S., Qiu, J., Li, J., & Yang, E. H. (2017). Strain hardening ultra-high performance concrete (SHUHPC) incorporating CNF-coated polyethylene fibers. *Cement and Concrete Research*, 98, 50-60.

19. Huang, B. T., Weng, K. F., Zhu, J. X., Xiang, Y., Dai, J. G., & Li, V. C. (2021). Engineered/strain-hardening cementitious composites (ECC/SHCC) with an ultra-high compressive strength over 210 MPa. *Composites Communications*, 26, 100775.

20. Yu, K., Wang, Y., Yu, J., & Xu, S. (2017). A strain-hardening cementitious composites with the tensile capacity up to 8%. *Construction and Building Materials*, 137, 410-419.

21. Shen, X., & Brühwiler, E. (2020). Influence of local fiber distribution on tensile behavior of strain hardening UHPFRC using NDT and DIC. *Cement and Concrete Research*, 132, 106042.

22. Ye, Y. Y., Smith, S. T., Zeng, J. J., Zhuge, Y., & Quach, W. M. (2021). Novel ultra-high-performance concrete composite plates reinforced with FRP grid: Development and mechanical behaviour. *Composite Structures*, 269, 114033.

23. Liao, J., Yang, K. Y., Zeng, J. J., Quach, W. M., Ye, Y. Y., & Zhang, L. (2021). Compressive behavior of FRP-confined ultra-high performance concrete (UHPC) in circular columns. *Engineering Structures*, 249, 113246.

24. Huang, B. T., Wang, Y. T., Wu, J. Q., Yu, J., Dai, J. G., & Leung, C. K. (2021). Effect of fiber content on mechanical performance and cracking characteristics of ultra-high-performance seawater sea-sand concrete (UHP-SSC). *Advances in Structural Engineering*, 24(6), 1182-1195.

25. Shen M. L., Zhou L. X., Chen Z. Y., Shen Y. N., Huang, B. T., & Lv, J. F. (2022). Effects of basalt powder and silica fume on ultra-high-strength cementitious matrix: A comparative study. *Case Studies in Construction Materials*, 17, e01397.

26. Wille, K., Kim, D. J., & Naaman, A. E. (2011). Strain-hardening UHP-FRC with low fiber contents. *Materials and Structures*, 44(3), 583-598.

27. Zhu, J. X., Xu, L. Y., Huang, B. T., Weng, K. F., & Dai, J. G. (2022). Recent developments in Engineered/Strain-Hardening Cementitious Composites (ECC/SHCC) with high and ultra-high strength. *Construction and Building Materials*, 342, 127956.

28. Lao, J. C., Xu, L. Y., Huang, B. T., Dai, J. G., & Shah, S. P. (2022). Strain-hardening Ultra-High-Performance Geopolymer Concrete (UHPGC): Matrix design and effect of steel fibers. Composites Communications, 30, 101081.

29. Huang, B. T., Zhu, J. X., Weng, K. F., Li, V. C., & Dai, J. G. (2022). Ultra-high-strength engineered/strain-hardening cementitious composites (ECC/SHCC): Material design and effect of fiber hybridization. *Cement and Concrete Composites*, 129, 104464.

30. Yu, K. Q., Zhu, W. J., Ding, Y., Lu, Z. D., Yu, J. T., & Xiao, J. Z. (2019). Micro-structural and mechanical properties of ultra-high performance engineered cementitious composites (UHP-ECC) incorporation of recycled fine powder (RFP). *Cement and Concrete Research*, 124, 105813.

31. Guan, X., Li, Y., Liu, T., Zhang, C., Li, H., & Ou, J. (2019). An economical ultra-high ductile engineered cementitious composite with large amount of coarse river sand. *Construction and Building Materials*, 201, 461-472.

32. Li, Y., Li, J., Yang, E. H., & Guan, X. (2022). Mechanism study of crack propagation in river sand Engineered Cementitious Composites (ECC). *Cement and Concrete Composites*, 128, 104434.

33. Li, Y., Li, J., Yang, E. H., & Guan, X. (2021). Investigation of matrix cracking properties of engineered cementitious composites (ECCs) incorporating river sands. *Cement and Concrete Composites*, 123, 104204.

34. Huang, B. T., Yu, J., Wu, J. Q., Dai, J. G., & Leung, C. K. (2020). Seawater sea-sand Engineered Cementitious Composites (SS-ECC) for marine and coastal applications. *Composites Communications*, 20, 100353.

35. Huang, B. T., Wu, J. Q., Yu, J., Dai, J. G., & Leung, C. K. (2020). High-strength seawater sea-sand Engineered Cementitious Composites (SS-ECC): Mechanical performance and probabilistic modeling. *Cement and Concrete Composites*, 114, 103740.

36. Almadani, M., Razak, R. A., Abdullah, M. M. A. B., & Mohamed, R. (2022). Geopolymer-Based Artificial Aggregates: A Review on Methods of Producing, Properties, and Improving Techniques. *Materials*, 15(16), 5516.

37. Tian, K., Wang, Y., Hong, S., Zhang, J., Hou, D., Dong, B., & Xing, F. (2021). Alkali-activated artificial aggregates fabricated by red mud and fly ash: Performance and microstructure. *Construction and Building Materials*, 281, 122552.

38. Dong, B., Chen, C., Wei, G., Fang, G., Wu, K., & Wang, Y. (2022). Fly ash-based artificial aggregates synthesized through alkali-activated cold-bonded pelletization technology. *Construction and Building Materials*, 344, 128268.

39. Peng, K. D., Huang, J. Q., Huang, B. T., Xu, L. Y., & Dai, J. G. (2023). Shear Strengthening of Reinforced Concrete Beams Using Geopolymer-Bonded Small-Diameter FRP Bars. *Composite Structures*, 305, 116513.

40. Peng, K. D., Huang, B. T., Xu, L. Y., Hu, R. L., & Dai, J. G. (2022). Flexural strengthening of reinforced concrete beams using geopolymer-bonded small-diameter CFRP bars. *Engineering Structures*, 256, 113992.

41. Xu, L. Y., Alrefaei, Y., Wang, Y. S., & Dai, J. G. (2021). Recent advances in molecular dynamics

simulation of the NASH geopolymer system: modeling, structural analysis, and dynamics. *Construction and Building Materials*, 276, 122196.

42. Luo, Q., Wang, Y., Hong, S., Xing, F., & Dong, B. (2021). Properties and microstructure of lithium-slag-based geopolymer by one-part mixing method. *Construction and Building Materials*, 273, 121723.
43. Qian, L. P., Xu, L. Y., Alrefaei, Y., Wang, T., Ishida, T., and Dai, J. G. (2022). Artificial alkali-activated aggregates developed from wastes and by-products: A state-of-the-art review. *Resources, Conservation and Recycling*, 177, 105971.
44. Xu, L. Y., Qian, L. P., Huang, B. T., & Dai, J. G. (2021). Development of artificial one-part geopolymer lightweight aggregates by crushing technique. *Journal of Cleaner Production*, 315, 128200.
45. Nadesan, M. S., & Dinakar, P. (2017). Structural concrete using sintered flyash lightweight aggregate: A review. *Construction and Building Materials*, 154, 928-944.
46. Ramamurthy, K., & Harikrishnan, K. I. (2006). Influence of binders on properties of sintered fly ash aggregate. *Cement and Concrete Composites*, 28(1), 33-38.
47. Tajra, F., Abd Elrahman, M., & Stephan, D. (2019). The production and properties of cold-bonded aggregate and its applications in concrete: A review. *Construction and Building Materials*, 225, 29-43.
48. Gesoğlu, M., Özturan, T., & Güneyisi, E. (2007). Effects of fly ash properties on characteristics of cold-bonded fly ash lightweight aggregates. *Construction and Building Materials*, 21(9), 1869-1878.
49. Liu, J., Li, Z., Zhang, W., Jin, H., Xing, F., Chen, C., ... & Wang, Y. (2022). Valorization of municipal solid waste incineration bottom ash (MSWIBA) into cold-bonded aggregates (CBAs): Feasibility and influence of curing methods. *Science of The Total Environment*, 843, 157004.
50. Yliniemi, Paiva, Ferreira, Tiainen, & Illikainen. (2017). Development and incorporation of lightweight waste-based geopolymer aggregates in mortar and concrete. *Construction and Building Materials*, 131, 784-792.
51. Qian, L. P., Xu, L. Y., Huang, B. T., & Dai, J. G. (2022). Pelletization and properties of artificial lightweight geopolymer aggregates (GPA): One-part vs. two-part geopolymer techniques. *Journal of Cleaner Production*, 374, 133933.
52. Wang, S., & Li, V. C. (2004). Tailoring of pre-existing flaws in ECC matrix for saturated strain hardening. In: *Proceedings of FRAMCOS-5*, Li et al. (eds), 1005–1012.
53. Li, V. C., & Wang, S. (2006). Microstructure variability and macroscopic composite properties of high performance fiber reinforced cementitious composites. *Probabilistic Engineering Mechanics*, 21(3), 201-206.
54. Yu, K., Zhu, H., Hou, M., & Li, V. C. (2021). Self-healing of PE-fiber reinforced lightweight high-strength engineered cementitious composite. *Cement and Concrete Composites*, 123, 104209.
55. Xu, L. Y., Huang, B. T., & Dai, J. G. (2021). Development of engineered cementitious composites (ECC) using artificial fine aggregates. *Construction and Building Materials*, 305, 124742.

56. Xu, L. Y., Huang, B. T., Li, V. C., & Dai, J. G. (2022). High-strength high-ductility Engineered/Strain-Hardening Cementitious Composites (ECC/SHCC) incorporating geopolymer fine aggregates. *Cement and Concrete Composites*, 125, 104296.

57. Xu, L. Y., Huang, B. T., Lao, J. C., & Dai, J. G. (2022). Tailoring strain-hardening behavior of high-strength Engineered Cementitious Composites (ECC) using hybrid silica sand and artificial geopolymer aggregates. *Materials & Design*, 220, 110876.

58. Xu, L. Y., Huang, B. T., Lan-Ping, Q., & Dai, J. G. (2022). Enhancing long-term tensile performance of Engineered Cementitious Composites (ECC) using sustainable artificial geopolymer aggregates. *Cement and Concrete Composites*, 133, 104676.

59. ASTM C618 - 19, Standard Specification for Coal Fly Ash and Raw or Calcined Natural Pozzolan for Use in Concrete, *ASTM International*, West Conshohocken, PA, 2019.

60. Nedeljković, M., Ghiassi, B., van der Laan, S., Li, Z., & Ye, G. (2019). Effect of curing conditions on the pore solution and carbonation resistance of alkali-activated fly ash and slag pastes. *Cement and Concrete Research*, 116, 146-158.

61. Xiang, Y., Fang, Z., Wang, C., Zhang, Y., & Fang, Y. (2017). Experimental investigations on impact behavior of CFRP cables under pretension. *Journal of Composites for Construction*, 21(2), 04016087.

62. Xiang, Y., Fang, Z., & Fang, Y. (2017). Single and multiple impact behavior of CFRP cables under pretension. *Construction and Building Materials*, 140, 521-533.

63. GB/T 14684-2011. (2011). *Sand for construction*, Standardization Administration of People's Republic of China, Beijing, China. (In Chinese)

64. Li, S., Chan, T. M., & Young, B. (2023). Experimental investigation on axial compressive behavior of novel FRP-ECC-HSC composite short column. *Composite Structures*, 303, 116285.

65. Li, S., Chan, T. M., & Young, B. (2022). Behavior of GFRP-concrete double tube composite columns. *Thin-Walled Structures*, 178, 109490.

66. ASTM C1437. (2020). *Standard Test Method for Flow of Hydraulic Cement Mortar*. ASTM International, West Conshohocken, PA.

67. GB/T 50080-2016. (2016). Standard for test method of performance on ordinary fresh concrete. Ministry of Housing and Urban-Rural Development of the People's Republic of China, Beijing, China. (In Chinese)

68. Wu, H. L., Zhang, D., Du, Y. J., & Li, V. C. (2020). Durability of engineered cementitious composite exposed to acid mine drainage. *Cement and Concrete Composites*, 108, 103550.

69. Wu, H. L., Yu, J., Zhang, D., Zheng, J. X., & Li, V. C. (2019). Effect of morphological parameters of natural sand on mechanical properties of engineered cementitious composites. *Cement and Concrete Composites*, 100, 108-119.

70. Oliver, W. C., & Pharr, G. M. (1992). An improved technique for determining hardness and elastic modulus using load and displacement sensing indentation experiments. *Journal of Materials Research*,

7(6), 1564-1583.

71. Oliver, W. C., & Pharr, G. M. (2004). Measurement of hardness and elastic modulus by instrumented indentation: Advances in understanding and refinements to methodology. *Journal of Materials Research*, 19(1), 3-20.

72. ASTM C469/C469M-14. (2014). Standard Test Method for Static Modulus of Elasticity and Poisson's Ratio of Concrete in Compression, *ASTM International*, West Conshohocken, PA.

73. Huang, B. T., Dai, J. G., Weng, K. F., Zhu, J. X., & Shah, S. P. (2021). Flexural performance of UHPC–concrete–ECC composite member reinforced with perforated steel plates. *Journal of Structural Engineering*, 147(6), 04021065.

74. Li, Q. H., Yin, X., Huang, B. T., Luo, A. M., Lyu, Y., Sun, C. J., & Xu, S. L. (2021). Shear Interfacial Fracture of Strain-Hardening Fiber-Reinforced Cementitious Composites and Concrete: A Novel Approach. *Engineering Fracture Mechanics*, 107849.

75. Fang, G., & Zhang, M. (2020). Multiscale micromechanical analysis of alkali-activated fly ash-slag paste. *Cement and Concrete Research*, 135, 106141.

76. Huang, H., Teng, L., Gao, X., Khayat, K. H., Wang, F., & Liu, Z. (2022). Effect of carbon nanotube and graphite nanoplatelet on composition, structure, and nano-mechanical properties of CSH in UHPC. *Cement and Concrete Research*, 154, 106713.

77. Vandamme, M., Ulm, F. J., & Fonollosa, P. (2010). Nanogranular packing of C–S–H at substochiometric conditions. *Cement and Concrete Research*, 40(1), 14-26.

78. Nedeljković, M., Ghiassi, B., & Ye, G. (2021). Role of curing conditions and precursor on the microstructure and phase chemistry of alkali-activated fly ash and slag pastes. *Materials*, 14(8), 1918.

79. Lu, C., Li, V. C., & Leung, C. K. (2018). Flaw characterization and correlation with cracking strength in Engineered Cementitious Composites (ECC). *Cement and Concrete Research*, 107, 64-74.

80. ASTM E399-19 (2019). Standard Test Method for Plane-Strain Fracture Toughness KIc of Metallic Materials. *ASTM International*, West Conshohocken, PA.

81. Wu, C., Leung, C. K., & Li, V. C. (2018). Derivation of crack bridging stresses in engineered cementitious composites under combined opening and shear displacements. *Cement and Concrete Research*, 107, 253-263.

82. Liu, W. H., Zhang, L. W., & Liew, K. M. (2022). A cyclic plastic-damage multiphase model for evaluation of multiple cracking in strain hardening cementitious composites. *Journal of the Mechanics and Physics of Solids*, 158, 104692.

83. Pan, Z., Wu, C., Liu, J., Wang, W., & Liu, J. (2015). Study on mechanical properties of cost-effective polyvinyl alcohol engineered cementitious composites (PVA-ECC). *Construction and Building Materials*, 78, 397-404.

84. Li, V. C., & Leung, C. K. (1992). Steady-state and multiple cracking of short random fiber composites. *Journal of Engineering Mechanics*, 118(11), 2246-2264.

85. Wu, H., Yu, J., Du, Y., & Li, V. C. (2021). Mechanical performance of MgO-doped engineered cementitious composites (ECC). *Cement and Concrete Composites*, 115, 103857.

86. Zhang, D., Yu, J., Wu, H., Jaworska, B., Ellis, B. R., & Li, V. C. (2020). Discontinuous micro-fibers as intrinsic reinforcement for ductile Engineered Cementitious Composites (ECC). *Composites Part B: Engineering*, 184, 107741.

87. Wu, H. C., & Li, V. C. (1992). Snubbing and bundling effects on multiple crack spacing of discontinuous random fiber-reinforced brittle matrix composites. *Journal of the American Ceramic Society*, 75(12), 3487-3489.

88. Ranade, R., Li, V. C., Stults, M. D., Rushing, T. S., Roth, J., & Heard, W. F. (2013). Micromechanics of high-strength, high-ductility concrete. *ACI Materials Journal*, 110(4), 375.

89. Aveston, J., Mercer, R. A., & Siltwood, J. M. (1974). Fiber reinforced cements—scientific foundations for specifications. *Composites standards testing arid design, Conference Proceedings National Physical Laboratory*, IPC Science and Technology Press, Guildford, United Kingdom, 93-103.

90. Li, V. C. (1992). Postcrack scaling relations for fiber reinforced cementitious composites. *Journal of Materials in Civil Engineering*, 4(1), 41-57.

91. Kanda, T., & Li, V. C. (1998). Multiple cracking sequence and saturation in fiber reinforced cementitious composites. *Concrete Research and Technology*, 9(2), 457-468.

92. ACI 318-14 (2011). Building Code Requirements for Structural Concrete and Commentary, American Concrete Institute, Detroit, Michigan.